Aerial Physical Interaction via IDA-PBC

Burak ¨ Yüksel, Cristian Secchi, Heinrich H Bülthoff, Antonio Franchi

HAL Id: hal-01964753

https://laas.hal.science/hal-01964753

Submitted on 23 Dec 2018

Aerial Physical Interaction via IDA-PBC

Burak Yüksel[1], Cristian Secchi[2], Heinrich H. Bülthoff[1] and Antonio Franchi[3]

Abstract

This paper proposes the use of a novel control method based on IDA-PBC in order to address the Aerial Physical Interaction (APhI) problem for a quadrotor UAV. The apparent physical properties of the quadrotor are reshaped in order to achieve better APhI performances, while ensuring the stability of the interaction through passivity preservation. The robustness of the IDA-PBC method with respect to sensor noise is also analyzed. The direct measurement of the external wrench – needed to implement the control method – is compared to the use of a nonlinear Lyapunov-based wrench observer and advantages/disadvantages of both methods are discussed. The validity and practicability of the proposed APhI method is evaluated through experiments, where for the first time in the literature, a light-weight all-in-one low-cost F/T sensor is used onboard of a quadrotor. Two main scenarios are shown: a quadrotor responding external disturbances while hovering (physical human-quadrotor interaction), and the same quadrotor sliding with a rigid tool along an uneven ceiling surface (inspection/painting-like task).

1 Introduction

Aerial physical interaction (APhI) is the field in which a flying robot maintains a stable flight while physically interacting with the environment. This is performed from the physics point of view by exerting meaningful forces and torques (wrenches) from the robot side to the environment, while the flying robot is accepting the wrench reactions in a stable and desired way.

Robots with flying capabilities, a.k.a. aerial robots, are appealing platforms for many researchers and engineers, because of their vast workspace (see Cai et al. (2014)). Especially the ones with stationary flight capacity, e.g., the Vertical Take-off and Landing (VTOL) vehicles, are progressively put in use for robotic tasks (e.g., helicopters as in Naldi (2008) or ducted-fan designs in Naldi et al. (2010)). VTOL robots provide the convenience of hovering around a fixed position, unlike the fixed-wing aerial robots, which require high cruise velocities for a stable flight. This ability of VTOLs makes them suitable platforms to be used for APhI or aerial manipulation tasks.

Quadrotors are one of the most cherished and preferred VTOL designs in the literature; primarily due to their symmetric design, simple mechanics and broad availability. Four symmetrically aligned pairwise counter rotating propellers allow quadrotors to move in the 3D space, which in the same time makes them underactuated systems. Although underactuation is a challenge for control of the mechanical systems (see Fantoni and Lozano (2002); Spong (1998)), it has certain benefits, e.g., it paves the way to low-weight and reduced-energy designs. Especially thanks to the underactuation, quadrotors can swiftly accelerate along the translational directions, hence perform agile motions (see Mahony et al. (2016)).

Aerial robots are used for many robotic tasks, e.g., for surveillance, monitoring, filming, etc. All these tasks have at least one thing in common: they avoid the obstacles, hence a physical interaction with their environment. Recently the need of APhI has emerged, where the flying robot is expected to exert meaningful wrenches to its environment while being resilient to the counter-wrenches (reactions) in a stable and desired way. Recently different methods and designs for addressing this non-trivial problem have been developed. In Augugliaro and DAndrea (2013) an admittance control framework presented, allowing quadrotors interact with humans, physically. The controller presented there is proposed for the partially linearized translational dynamics in near-hovering configuration of the robot, which provides a local solution in terms of physical interaction. A hybrid position and wrench control for quadrotors is presented in Bellens et al. (2012), where for dealing with poorly structured environment, an impedance control has been exploited. Authors of Gioioso et al. (2014) turned a standard near-hovering controller into a 3D force controller, and implemented it on a quadrotor for effectively exerting desired forces to its environment via a rigid tool. Using quadrotors equipped with rigid tools for APhI is further studied in Ha et al. (2015) and Nguyen and Lee (2013), where the nonlinear quadrotor dynamics is exploited for performing tool operations e.g., screw-driving. In Fumagalli et al. (2012b), researchers presented a design of a quadrotor VTOL

[1]Max Planck Institute for Biological Cybernetics, Spemanstr. 38, 72076, Tübingen, Germany.
[2]Universiy of Modena and Reggio Emilia, Reggio Emilia, Italy.
[3]LAAS-CNRS, Université de Toulouse, CNRS, Toulouse, France

for contact inspection purposes. The controller presented there is a *passivity-based* controller; shaping the potential energy of the quadrotor for setting a desired stiffness behavior[1] (see also Mersha et al. (2011)).

Developing controllers for nonlinear systems, which are enjoying the *passivity* property, has been one of the most evident method in the field of Control Theory (for more details on passivity and how it relates to the stability of the linear/nonlinear systems, see Khalil (2001), Sepulchre et al. (1997)). The *Interconnection and Damping Assignment - Passivity Based Control* (IDA-PBC) is one of the most powerful passivity-based control methods for controlling the interactive behavior of physical systems, which allows *shaping* the energetic properties of one or interconnected multi system(s) in a power-preserving manner, such that the conservation laws of the physics are respected (see the details and its applicability in Ortega et al. (2002)). Very recently it is adopted for controlling aerial robots as well. In Acosta et al. (2014) control of an aerial manipulator using IDA-PBC has been shown for tracking the desired trajectories of the Center of Mass (CoM) of the overall system. In Guerrero et al. (2015) IDA-PBC has been implemented for suppressing the swing of a cable attached to a quadrotor, which is carrying a load at the other end of the cable.

For the first time in the literature we have presented an IDA-PBC method for quadrotor UAVs for performing APhI tasks in Yüksel et al. (2014b), and in Yüksel et al. (2014a) we have proposed a novel wrench estimation technique to be exploited for APhI with IDA-PBC, where we have shown its effectiveness in simulations. Differently from the already existing methods, this IDA-PBC is developed purely for quadrotors enabling them for meaningful physical interactions with their environments for tasks, e.g. human-robot interaction or sliding, using a rigid tool for painting, cleaning or surface inspection. This journal paper is extending our previous work in various directions by: *i)* studying first time the robustness of this IDA-PBC method for the quadrotor UAVs w.r.t. measurement noise in form of (34) for all states and in form of (51) for external wrench measurements, *ii)* comparing experimentally the wrench estimation strategy proposed in Yüksel et al. (2014a) with a novel low-cost light-weight 6D F/T sensor mounted on a quadrotor. *iii)* implementing first time a low-cost, light-weight, all-in-one F/T sensor fully onboard of a free-flying quadrotor UAV for APhI tasks, *iv)* providing the first experimental results of this IDA-PBC method for demanding APhI tasks: human-robot interaction and sliding on an uneven ceiling surface.

The paper is organized as in the following. In Section 2.1 we informally recall the IDA-PBC method for port-Hamiltonian (PH) systems. Then in Sec. 2.2 we present the kinematics and dynamics of a quadrotor, where we rewrite its dynamics in PH form. In Section 2.3 we present the overall IDA-PBC method for quadrotor UAVs enabling them for APhI tasks. Section 2.4 is where we study the robustness of this controller against measurement noises, e.g., from sensors that are providing positions, orientations, their velocities and also the external force and torque values. In Section 3 both estimation and measurement methods of the external wrenches are presented. Here first a Lyapunov-based

nonlinear external wrench observer is recalled in Section 3.1 and in Section 3.2 we explain how to implement a light-weight all-in-one 6D F/T sensor onboard of a quadrotor. In Section 3.3 we compare the performances of these two methods over each other based on the experimental data and favor the use of F/T sensor for APhI experiments. The experimental results are provided in Section 4 for: *i)* shaping the rotational inertia of a quadrotor, *ii)* sliding on an uneven ceiling surface with a quadrotor equipped with a rigid tool, demonstrating the power of IDA-PBC for APhI task of the quadrotor UAVs and providing the experimental validation for our theoretical contribution.

2   IDA-PBC for Quadrotors

2.1   *Preliminaries on IDA-PBC*

Mechanical systems can be represented as port-Hamiltonian (PH) systems, a generalization of standard classical Hamiltonian mechanics where the energetic properties are evident. IDA-PBC is a passivity based control strategy that allows to assign to the controlled system a desired dynamics that can be still represented as a port-Hamiltonian system (see Ortega et al. (2002)).

The most common representation of a port-Hamiltonian system is the following:

$$
\begin{cases}
\dot{\mathbf{x}} = [\mathcal{J}(\mathbf{x}) - \mathcal{R}(\mathbf{x})] \frac{\partial H}{\partial \mathbf{x}} + \mathbf{G}(\mathbf{x})\mathbf{u} \\
\mathbf{y} = \mathbf{G}(\mathbf{x})^T \frac{\partial H}{\partial \mathbf{x}},
\end{cases} \tag{1}
$$

where $\mathbf{x} \in \mathbb{R}^n$ is the state and $H(\mathbf{x}) : \mathbb{R}^n \to \mathbb{R}_{\geq 0}$ represents the total amount of energy (*Hamiltonian*) stored in the system. Matrices $\mathcal{J}(\mathbf{x}) = -\mathcal{J}(\mathbf{x})^T$ and $\mathcal{R}(\mathbf{x}) \geq 0$ represent the internal energetic interconnections and the dissipation of the port-Hamiltonian system, respectively. Furthermore, $\mathbf{G}(\mathbf{x})$ is the input matrix and the input-output pair $\langle \mathbf{u}, \mathbf{y} \rangle$ represents a power port, namely a pair of variables whose product gives the (generalized) power that is either stored or dissipated by the system. A port-Hamiltonian system is passive with respect to the pair $\langle \mathbf{u}, \mathbf{y} \rangle$ (for more details see, e.g., Secchi et al. (2007)).

Then, using IDA-PBC from Ortega et al. (2002) and its extension proposed in Wang et al. (2009), it is possible to control a port-Hamiltonian system in such a way that it behaves with a certain target dynamics, i.e., like a new port-Hamiltonian system with a desired interconnection matrix, damping matrix and energy function and even with a different state variable $\bar{\mathbf{x}} \in \mathbb{R}^n$. As reported in Yüksel et al. (2014b), let

$$
\mathbf{x} = \boldsymbol{\Phi}(\bar{\mathbf{x}}, t) \tag{2}
$$

be the map relating $\bar{\mathbf{x}}$ and $\mathbf{x}$, where $\boldsymbol{\Phi}$ and $\frac{\partial \boldsymbol{\Phi}}{\partial \bar{\mathbf{x}}}$ are invertible at any time t. Let $\mathcal{J}_d$, $\mathcal{R}_d$ and H_d be the desired interconnection matrix, dissipation matrix and energy function, respectively. The port-Hamiltonian system in (1) can be transformed into the target port-Hamiltonian dynamics described by

$$
\dot{\mathbf{x}} = [\mathcal{J}_d(\bar{\mathbf{x}}) - \mathcal{R}_d(\bar{\mathbf{x}})] \frac{\partial H_d}{\partial \bar{\mathbf{x}}} \tag{3}
$$

$$\mathbf{u} = \begin{bmatrix} u_t \\ \hline \mathbf{u}_r \end{bmatrix} = \begin{bmatrix} u_t \\ \hline u_\phi \\ u_\theta \\ u_\psi \end{bmatrix} = \begin{bmatrix} c_f & c_f & c_f & c_f \\ 0 & 0 & -d_p c_f & d_p c_f \\ d_p c_f & -d_p c_f & 0 & 0 \\ -c_t & -c_t & c_t & c_t \end{bmatrix} \begin{bmatrix} \Omega_1^2 \\ \Omega_2^2 \\ \Omega_3^2 \\ \Omega_4^2 \end{bmatrix}$$
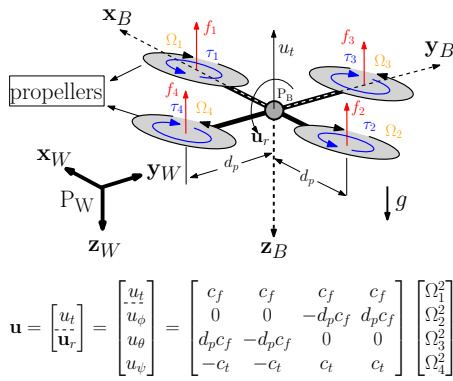
Figure 1. A sketch of a quadrotor. Four propellers are placed symmetrically on the body frame at a distance of $d_p \in \mathbb{R}^+$ from the CoM (P_B). Each propeller rotates with a velocity $\Omega_i \in \mathbb{R}$ in opposite direction w.r.t. its neighbor. Due to the design of the propellers, each of them generates a trust force $f_i \in \mathbb{R}$ and a drag torque $\tau_i \in \mathbb{R}$. Notice that these forces and torques are coupled, since $f_i = c_f \Omega_i^2$ and $\tau_i = c_t \Omega_i^2$ holds. Hence the system is underactuated with four control inputs $\{\Omega_1, \Omega_2, \Omega_3, \Omega_4\}$, and it is trivial to find the constant mapping from these velocities to $\mathbf{u} \in \mathbb{R}^4$ of the system dynamics in Section 2.2.

using

$$\mathbf{u} = \mathbf{G}^+(\mathbf{x}) \left[\frac{\partial \mathbf{\Phi}}{\partial \bar{\mathbf{x}}} (\mathcal{J}_d(\bar{\mathbf{x}}) - \mathcal{R}_d(\bar{\mathbf{x}})) \frac{\partial H_d}{\partial \bar{\mathbf{x}}} \right.$$
$$\left. - (\mathcal{J}(\mathbf{x}) - \mathcal{R}(\mathbf{x})) \frac{\partial H}{\partial \mathbf{x}} + \frac{\partial \mathbf{\Phi}}{\partial t} \right], \quad (4)$$

where $\mathbf{G}^+(\mathbf{x}) = (\mathbf{G}^T(\mathbf{x})\mathbf{G}(\mathbf{x}))^{-1}\mathbf{G}^T(\mathbf{x})$ is the pseudo-inverse of $\mathbf{G}(\mathbf{x})$, if and only if the following *matching equation* holds:

$$\mathbf{G}^\perp(\mathbf{x}) \left[\frac{\partial \mathbf{\Phi}}{\partial \bar{\mathbf{x}}} (\mathcal{J}_d(\bar{\mathbf{x}}) - \mathcal{R}_d(\bar{\mathbf{x}})) \frac{\partial H_d}{\partial \bar{\mathbf{x}}} + \right.$$
$$\left. + \frac{\partial \mathbf{\Phi}}{\partial t} - (\mathcal{J}(\mathbf{x}) - \mathcal{R}(\mathbf{x})) \frac{\partial H}{\partial \mathbf{x}} \right] = \mathbf{0}, \quad (5)$$

where $\mathbf{G}^\perp(\mathbf{x})$ is the full rank left annihilator of $\mathbf{G}(\mathbf{x})$.

2.2 Quadrotor Model and its PH Form

A sketch of a quadrotor is presented in Fig. 1, where $\mathcal{F}_W : \{P_W, \mathbf{x}_W, \mathbf{y}_W, \mathbf{z}_W\}$ is the world frame, $\mathcal{F}_B : \{P_B, \mathbf{x}_B, \mathbf{y}_B, \mathbf{z}_B\}$ is the body-fixed frame whose origin P_B is the CoM of the quadrotor. The orientation of $\mathcal{F}_B$ in $\mathcal{F}_W$ is represented with a rotation matrix $\mathbf{R}(\boldsymbol{\eta}) \in SO(3)$, which is a function of $\boldsymbol{\eta} = [\phi \ \theta \ \psi]^T \in \mathbb{R}^3$ (roll-pitch-yaw angles) that is a minimal representation of the orientation. The gravity vector is facing $+\mathbf{z}_W$ and its intensity is $g \in \mathbb{R}$.

The dynamics of a quadrotor is well-known, see, e.g., Yüksel et al. (2014b). The translational one can be written as

$$\Sigma_t : \left\{ m\ddot{\mathbf{p}}_q = -u_t \mathbf{R}(\boldsymbol{\eta})\mathbf{e}_3 + mg\mathbf{e}_3 + \mathbf{f}_{ext}, \quad (6) \right.$$

where $\mathbf{p}_q = [x_q \ y_q \ z_q]^T \in \mathbb{R}^3$ is the Cartesian position of P_B in $\mathcal{F}_W$, $m \in \mathbb{R}^+$ is the mass of the quadrotor, $u_t \in \mathbb{R}$ is the intensity of the total thrust force of the propellers acting at P_B, $\mathbf{f}_{ext} \in \mathbb{R}^3$ represents the external forces acting at P_B

in $\mathcal{F}_W$, and $\mathbf{e}_3 = [0 \ 0 \ 1]^T$. The rotational dynamics is

$$\Sigma_r : \begin{cases} \mathbf{M}_{qr}\dot{\boldsymbol{\omega}} & = [\boldsymbol{\omega}]_\wedge \mathbf{M}_{qr}\boldsymbol{\omega} + \mathbf{u}_r + \boldsymbol{\tau}_{ext} \\ \dot{\boldsymbol{\eta}} & = \mathbf{T}(\boldsymbol{\eta})\boldsymbol{\omega}, \end{cases} \quad (7)$$

where $\mathbf{M}_{qr} \in \mathbb{R}^{3\times3}$ is the rotational inertia matrix, $\boldsymbol{\omega} \in \mathbb{R}^3$ is the body-frame angular velocitiy represented in $\mathcal{F}_B$, $\mathbf{T}(\boldsymbol{\eta}) \in \mathbb{R}^{3\times3}$ is the transformation matrix from $\boldsymbol{\omega}$ to the Euler rates $\dot{\boldsymbol{\eta}}$, $\mathbf{u}_r \in \mathbb{R}^3$ is the total torque input expressed in $\mathcal{F}_B$, and $\boldsymbol{\tau}_{ext} \in \mathbb{R}^3$ is the total external torque. The four-dimensional control input of the quadrotor is denoted with $\mathbf{u} = [u_t \ \mathbf{u}_r^T]^T \in \mathbb{R}^4$, and the external wrench with $\mathbf{w}_{ext} = [\mathbf{f}_{ext}^T \ \boldsymbol{\tau}_{ext}^T]^T \in \mathbb{R}^6$. Finally, $[\star]_\wedge : \mathbb{R}^3 \to so(3)$ is the skew-symmetric operator.

For implementing the IDA-PBC on the quadrotor, we first bring the quadrotor dynamics into a PH-formalization[2]. For this reason, we consider a pre-compensating control input (similar to the one in Lee et al. (2013) and also see Fig. 2) in the form of

$$\mathbf{u}_r = \mathbf{M}_{qr}\mathbf{T}^{-1} \left[(-k_d\mathbf{I} + \mathbf{Q})\dot{\boldsymbol{\eta}} + \bar{\mathbf{u}}_r + (\mathbf{I} - \mathbf{M}_{qr}^{-1})\boldsymbol{\tau}_{ext} \right]$$
$$\mathbf{Q} = \mathbf{T}\dot{\mathbf{T}}^{-1} + \mathbf{T}\mathbf{M}_{qr}^{-1}[\boldsymbol{\omega}]_\wedge \mathbf{M}_{qr}\mathbf{T}^{-1}, \quad (8)$$

where $\mathbf{I}$ is the identity matrix with proper dimension and $k_d \in \mathbb{R}^+$. Substituting (8) in (7), we get

$$\ddot{\boldsymbol{\eta}} = -k_d\dot{\boldsymbol{\eta}} + \bar{\mathbf{u}}_r + \boldsymbol{\tau}_{ext}. \quad (9)$$

Hence, after the pre-compensation given in (8), the quadrotor dynamics is defined by (6) and (9). This new system can be modeled as a mechanical port-Hamiltonian system. Let be $\mathbf{M} = \text{diag}([m\mathbf{I}, \mathbf{I}]) \in \mathbb{R}^{6\times6}$ and define $\mathbf{q} = [\mathbf{p}_q^T \ \boldsymbol{\eta}^T]^T = [q_1 \cdots q_6]^T \in \mathbb{R}^6$ and $\mathbf{p} = \mathbf{M}\dot{\mathbf{q}} \in \mathbb{R}^6$ as the the configuration and momentum variables, respectively. Furthermore, let $\mathbf{u}_i = [u_t \ \bar{\mathbf{u}}_r^T]^T \in \mathbb{R}^4$ be the input vector (see in Fig. 2 for how $\mathbf{u}_i$ enters the controller). The dynamics (6) and (9), can be rewritten as:

$$\begin{bmatrix} \dot{\mathbf{q}} \\ \dot{\mathbf{p}} \end{bmatrix} = \left[\begin{pmatrix} \mathbf{0} & \mathbf{I} \\ -\mathbf{I} & \mathbf{0} \end{pmatrix} - \begin{pmatrix} \mathbf{0} & \mathbf{0} \\ \mathbf{0} & \mathcal{R} \end{pmatrix} \right] \begin{bmatrix} \frac{\partial H}{\partial \mathbf{q}} \\ \frac{\partial H}{\partial \mathbf{p}} \end{bmatrix} + $$
$$+ \begin{bmatrix} \mathbf{0} & \mathbf{0} \\ \mathbf{G} & \mathbf{I} \end{bmatrix} \begin{bmatrix} \mathbf{u}_i \\ \mathbf{w}_{ext} \end{bmatrix}, \quad (10)$$

where $\mathcal{R} = k_d\mathbf{I}$ models the dissipation introduced by (8), and $\mathbf{I}$ and $\mathbf{0}$ stand for the identity and zero matrices of proper dimensions, respectively. The total energy function and the control input matrix $\mathbf{G}$ are given by:

$$H(\mathbf{q}, \mathbf{p}) = \frac{1}{2}\mathbf{p}^T\mathbf{M}^{-1}\mathbf{p} + V(\mathbf{q}) = \frac{1}{2}\mathbf{p}^T\mathbf{M}^{-1}\mathbf{p} - mgq_3, \quad (11)$$

$$\mathbf{G} = \begin{bmatrix} \mathbf{g}_1 & \mathbf{0} \\ \mathbf{0} & \mathbf{I} \end{bmatrix} \in \mathbb{R}^{6\times4} \quad \text{with} \quad \mathbf{g}_1 = -\mathbf{R}\mathbf{e}_3 \in \mathbb{R}^3. \quad (12)$$

The following Proposition holds.

Proposition 1. *The system* (10) *is cyclo-passive with respect to the pair*

$$\left\langle \begin{bmatrix} \mathbf{u}_i \\ \mathbf{w}_{ext} \end{bmatrix}, \begin{bmatrix} \mathbf{G}^T \frac{\partial H}{\partial \mathbf{p}} \\ \frac{\partial H}{\partial \mathbf{p}} \end{bmatrix} \right\rangle.$$
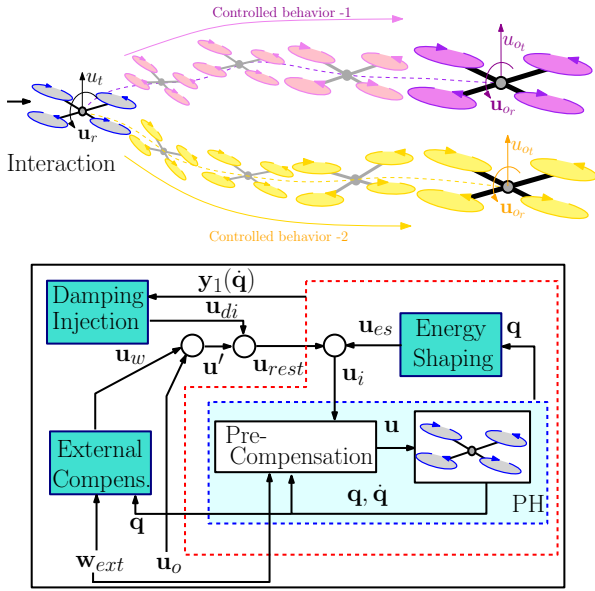
Figure 2. Above: a sketch illustrating pictorially the idea of possibly transforming the quadrotor into two quadrotors with apparent different dynamics that react as two new physical systems to the external solicitation.
Below: IDA-PBC controller scheme, where the pre-compensating control input is computed using (8) and all other blocks are explained in Section 2.3 in detail.

Proof. Consider the energy function defined in (11). Using (10) we obtain

$$
\dot{H} = \begin{bmatrix} \frac{\partial^T H}{\partial \mathbf{q}} & \frac{\partial^T H}{\partial \mathbf{p}} \end{bmatrix} \begin{bmatrix} \dot{\mathbf{q}} \\ \dot{\mathbf{p}} \end{bmatrix}
$$
$$
= -\frac{\partial^T H}{\partial \mathbf{p}} \mathcal{R} \frac{\partial H}{\partial \mathbf{p}} + \frac{\partial^T H}{\partial \mathbf{p}} \mathbf{G}\mathbf{u}_i + \frac{\partial^T H}{\partial \mathbf{p}} \mathbf{w}_{ext}. \quad (13)
$$

Considering that $\mathcal{R} \geq \mathbf{0}$ we obtain

$$
\dot{H} \leq \frac{\partial^T H}{\partial \mathbf{p}} \mathbf{G}\mathbf{u}_i + \frac{\partial^T H}{\partial \mathbf{p}} \mathbf{w}_{ext} \quad (14)
$$

which proves the statement. ∎

Cyclo-passivity is as an extension of the passivity property, which requires the system to behave as a physical one from an energetic point of view (i.e., that the energy introduced into the system from the external world is either stored or dissipated) but does not require the energy function being lower bounded. Meticulous reader can refer to Willems (1972) for more details on cyclo-passivity.

2.3 IDA-PBC Framework

Now let us show how one can use IDA-PBC method for bringing the original system dynamics (10) into the desired (target) one

$$
\begin{bmatrix} \dot{\mathbf{q}} \\ \dot{\bar{\mathbf{p}}} \end{bmatrix} = \left[\begin{pmatrix} \mathbf{0} & \mathbf{I} \\ -\mathbf{I} & \mathbf{0} \end{pmatrix} - \begin{pmatrix} \mathbf{0} & \mathbf{0} \\ \mathbf{0} & \mathcal{R}_d \end{pmatrix} \right] \begin{bmatrix} \frac{\partial H_d}{\partial \mathbf{q}} \\ \frac{\partial H_d}{\partial \bar{\mathbf{p}}} \end{bmatrix} + \begin{bmatrix} \mathbf{0} \\ \mathbf{I} \end{bmatrix} \bar{\mathbf{w}}_{ext},
$$
$$
\quad (15)
$$

where $\bar{\mathbf{p}} = \mathbf{M}_d \dot{\mathbf{q}}$ is the new momentum associated to the new inertia matrix $\mathbf{M}_d = \mathrm{diag}([m_d \mathbf{I}, \mathbf{N}]) \in \mathbb{R}^{6 \times 6}$, $m_d \in \mathbb{R}^+$ is the desired mass, and $\mathbf{N} \in \mathbb{R}^{3 \times 3}$ is a positive definite desired

rotational inertia matrix. The desired energy function is

$$
H_d = \frac{1}{2} \bar{\mathbf{p}}^T \mathbf{M}_d \bar{\mathbf{p}} + V_d(\mathbf{q}), \quad (16)
$$

where V_d is the desired potential energy satisfying the matching condition of IDA-PBC (see (5)). The desired dissipation matrix $\mathcal{R}_d$ has to be designed in order to assign a wished viscous behavior to the new quadrotor dynamics, while taking its underactuation into account. Finally $\bar{\mathbf{w}}_{ext} \in \mathbb{R}^6$ is the best external wrench compensation that can be achieved considering the underactuation of the system.

The goal of imposing the different target dynamics given in (15) is to let the system react in a different (desired) way to the external solicitations, as if it was a physically different system. Here we briefly recall the main steps for building the IDA-PBC controller for quadrotors. A more detailed description can be found in Yüksel et al. (2014b).

The IDA-PBC control input is $\mathbf{u}_i = \mathbf{u}_{es} + \mathbf{u}_{di} + \mathbf{u}_w + \mathbf{u}_o$, where the four low-level control inputs are defined as: *i)* $\mathbf{u}_{es}$: energy shaping input, *ii)* $\mathbf{u}_{di}$: damping injection input, *iii)* $\mathbf{u}_w$: external wrench compensation input, and *iv)* an additional *high-level* control input, $\mathbf{u}_o \in \mathbb{R}^4$, which can be used for, e.g., position or force/torque tracking. See also Fig. 2 for a sketch showing how all these control inputs are combined.

We start showing the computation of the energy shaping control input.

2.3.1 Energy Shaping: Consider the original system dynamics (10) in absence of any dissipative elements and for now not considering any external disturbances:

$$
\begin{bmatrix} \dot{\mathbf{q}} \\ \dot{\mathbf{p}} \end{bmatrix} = \begin{bmatrix} \mathbf{0} & \mathbf{I} \\ -\mathbf{I} & \mathbf{0} \end{bmatrix} \begin{bmatrix} \frac{\partial H}{\partial \mathbf{q}} \\ \frac{\partial H}{\partial \mathbf{p}} \end{bmatrix} + \begin{bmatrix} \mathbf{0} \\ \mathbf{G} \end{bmatrix} \mathbf{u}_{es}, \quad (17)
$$

where the input $\mathbf{u}_{es}$ has to be designed in order to obtain an undamped controlled system with the desired energy function H_d and with the desired momentum $\bar{\mathbf{p}}$, i.e., to obtain:

$$
\begin{bmatrix} \dot{\mathbf{q}} \\ \dot{\bar{\mathbf{p}}} \end{bmatrix} = \begin{bmatrix} \mathbf{0} & \mathbf{I} \\ -\mathbf{I} & \mathbf{0} \end{bmatrix} \begin{bmatrix} \frac{\partial H_d}{\partial \mathbf{q}} \\ \frac{\partial H_d}{\partial \bar{\mathbf{p}}} \end{bmatrix}. \quad (18)
$$

It has been shown in Yüksel et al. (2014b) that for the system at hand, the map (2) relating $\mathbf{x} = [\mathbf{q}^T \ \mathbf{p}^T]^T$ to $\bar{\mathbf{x}} = [\mathbf{q}^T \ \bar{\mathbf{p}}^T]^T$ is actually

$$
\mathbf{x} = \mathbf{\Phi}(\bar{\mathbf{x}}), \quad \mathbf{\Phi}(\bar{\mathbf{x}}) = \mathbf{F}\bar{\mathbf{x}}, \quad \mathbf{F} = \begin{bmatrix} \mathbf{I} & \mathbf{0} \\ \mathbf{0} & \mathbf{M}\mathbf{M}_d^{-1} \end{bmatrix}, \quad (19)
$$

which implies that $\frac{\partial \mathbf{\Phi}}{\partial \bar{\mathbf{x}}} = \mathbf{F}$, and $\frac{\partial \mathbf{\Phi}}{\partial t} = \mathbf{0}$. Under this circumstances, by choosing the energy shaping control input as

$$
\mathbf{u}_{es} = \mathbf{G}^+ \left(\frac{\partial H}{\partial \mathbf{q}} - \mathbf{M}\mathbf{M}_d^{-1} \frac{\partial H_d}{\partial \mathbf{q}} \right) \quad (20)
$$

we can modify the original undamped system (17) into the target dynamics (18) if and only if the matching condition given in (5) holds. In Yüksel et al. (2014b) we have shown that choosing

$$
V_d(\mathbf{q}) = -m_d g q_3 + \bar{V}_d(\boldsymbol{\eta}) \quad (21)
$$

is one way to meet (5), when there are no singularities in the quadrotor's configuration and $\bar{V}_d(\boldsymbol{\eta})$ is a 'well-behaved'[3]

energetic function from physics point of view, e.g.,

$$\bar{V}_d = \frac{1}{2}\boldsymbol{\eta}_e^T \mathbf{K}_p \boldsymbol{\eta}_e \tag{22}$$
$$\boldsymbol{\eta}_e = \boldsymbol{\eta} - \boldsymbol{\eta}^*,$$

where $\mathbb{R}^{3\times 3} \ni \mathbf{K}_p > \mathbf{0}$ and the desired attitude $\boldsymbol{\eta}^* = [\phi^*\ \theta^*\ \psi^*]^T \in \mathbb{R}^3$ is an orientation equilibrium away from singularities, where the rotational potential reaches its minimum.

Now we show how one can shape the dissipative behavior of the quadrotor by using damping injection.

2.3.2 Damping Injection: The IDA-PBC input can be written as $\mathbf{u}_i = \mathbf{u}_{es} + \mathbf{u}_{rest}$, where $\mathbf{u}_{rest} = \mathbf{u}_{di} + \mathbf{u}_w + \mathbf{u}_o$. In Yüksel et al. (2014b) it is shown that considering the mapping in (19) and the fact that $\frac{\partial H}{\partial \mathbf{p}} = \frac{\partial H_d}{\partial \bar{\mathbf{p}}}$, implementing the control input $\mathbf{u}_i = \mathbf{u}_{es} + \mathbf{u}_{rest}$ (considering also (20)) on the original system dynamics (10) will result in

$$\begin{bmatrix} \dot{\mathbf{q}}_q \\ \dot{\bar{\mathbf{p}}} \end{bmatrix} = \begin{bmatrix} \mathbf{0} & \mathbf{I} \\ -\mathbf{I} & \mathbf{0} \end{bmatrix} \begin{bmatrix} \frac{\partial H_d}{\partial \mathbf{q}} \\ \frac{\partial H_d}{\partial \bar{\mathbf{p}}} \end{bmatrix} - \begin{bmatrix} \mathbf{0} & \mathbf{0} \\ \mathbf{0} & \mathbf{M}_d \mathbf{M}^{-1}\mathcal{R} \end{bmatrix} \begin{bmatrix} \frac{\partial H}{\partial \mathbf{q}} \\ \frac{\partial H}{\partial \bar{\mathbf{p}}} \end{bmatrix} +$$
$$+ \begin{bmatrix} \mathbf{0} \\ \mathbf{M}_d\mathbf{M}^{-1}\mathbf{G} \end{bmatrix} \mathbf{u}_{rest} + \begin{bmatrix} \mathbf{0} \\ \mathbf{M}_d\mathbf{M}^{-1} \end{bmatrix} \mathbf{w}_{ext}. \tag{23}$$

Now decomposing the control input $\mathbf{u}_{rest} = \mathbf{u}_{di} + \mathbf{u}'$ with $\mathbf{u}' = \mathbf{u}_w + \mathbf{u}_o$ (see Fig. 2) and setting

$$\mathbf{u}_{di} = -\mathbf{K}_v \mathbf{y}_1, \tag{24}$$

where

$$\mathbf{y}_1 = \mathbf{G}^T \mathbf{M}^{-T} \mathbf{M}_d^T \frac{\partial H_d}{\partial \bar{\mathbf{p}}}, \quad \mathbf{K}_v = \begin{bmatrix} k_T & \mathbf{0} \\ \mathbf{0} & \mathbf{K}_R \end{bmatrix} \in \mathbb{R}^{4\times 4}$$

and implementing $\mathbf{u}_{di}$ in (23) we get

$$\begin{bmatrix} \dot{\mathbf{q}} \\ \dot{\bar{\mathbf{p}}} \end{bmatrix} = \left[\begin{pmatrix} \mathbf{0} & \mathbf{I} \\ -\mathbf{I} & \mathbf{0} \end{pmatrix} - \begin{pmatrix} \mathbf{0} & \mathbf{0} \\ \mathbf{0} & \mathcal{R}_d \end{pmatrix} \right] \begin{bmatrix} \frac{\partial H_d}{\partial \mathbf{q}} \\ \frac{\partial H_d}{\partial \bar{\mathbf{p}}} \end{bmatrix} +$$
$$+ \begin{bmatrix} \mathbf{0} \\ \mathbf{M}_d\mathbf{M}^{-1}\mathbf{G} \end{bmatrix} \mathbf{u}' + \begin{bmatrix} \mathbf{0} \\ \mathbf{M}_d\mathbf{M}^{-1} \end{bmatrix} \mathbf{w}_{ext}, \tag{25}$$

where $\mathcal{R}_d$ denotes the desired dissipation matrix, achieved via damping injection for assigning a target viscous behavior to the system.

Remark 1. *The choice of $\mathbf{K}_v \in \mathbb{R}^{4\times 4}$ in (24) has to be done in a way that the desired dissipation matrix $\mathcal{R}_d$ in (25) is positive definite. It was shown in Yüksel et al. (2014b) that this can be achieved for $\mathbf{K}_v = \mathrm{diag}([k_T\ \mathbf{K}_R])$, where $k_T \in \mathbb{R}^+$ and $\mathbb{R}^{3\times 3} \ni \mathbf{K}_R > 0$, with*

$$\begin{cases} k_T = \left(\frac{m}{m_d}\right)^2 \bar{k}_T \\ \mathbf{K}_R = \mathbf{N}^{-1}(\bar{\mathbf{K}}_R - k_d \mathbf{N})\mathbf{N}^{-1}, \end{cases} \tag{26}$$

for any $\bar{k}_T \in \mathbb{R}^+$ and $\mathbb{R}^{3\times 3} \ni \bar{\mathbf{K}}_R > \mathbf{0}$.

2.3.3 External Wrench Compensation: The change of the momentum for the desired (target) dynamics and the underactuation of the system introduces a scaling not only to the control of the system, but also to the way external wrench $\mathbf{w}_{ext}$ influences the evolution of the system.

Ideally this wrench should influence the controlled system dynamics in the same way it does for the original system given in (10). Hence a control action, called external wrench compensation, needs to be taken into account to eliminate this scaling. In Yüksel et al. (2014b) it was shown that this can be done by applying the following control input further in (25)

$$\mathbf{u}' = \mathbf{u}_w + \mathbf{u}_o$$
$$\mathbf{u}_w = \mathbf{G}^+(\mathbf{M}\mathbf{M}_d^{-1}(\mathbf{I} - \mathbf{M}_d\mathbf{M}^{-1})\mathbf{w}_{ext}), \tag{27}$$

which leads to the following closed-loop system

$$\begin{bmatrix} \dot{\mathbf{q}} \\ \dot{\bar{\mathbf{p}}} \end{bmatrix} = \left[\begin{pmatrix} \mathbf{0} & \mathbf{I} \\ -\mathbf{I} & \mathbf{0} \end{pmatrix} - \begin{pmatrix} \mathbf{0} & \mathbf{0} \\ \mathbf{0} & \mathcal{R}_d \end{pmatrix} \right] \begin{bmatrix} \frac{\partial H_d}{\partial \mathbf{q}} \\ \frac{\partial H_d}{\partial \bar{\mathbf{p}}} \end{bmatrix} +$$
$$+ \begin{bmatrix} \mathbf{0} \\ \mathbf{I} \end{bmatrix} \bar{\mathbf{w}}_{ext} + \begin{bmatrix} \mathbf{0} \\ \mathbf{M}_d\mathbf{M}^{-1}\mathbf{G} \end{bmatrix} \mathbf{u}_o, \tag{28}$$

that is the physically reshaped quadrotor with desired (target) dynamics. Notice that for $\mathbf{u}_o = \mathbf{0}$, (28) is identical to (15).

Summarizing, the IDA-PBC control input in form of

$$\mathbf{u}_i = \mathbf{u}_{es} + \mathbf{u}_{di} + \mathbf{u}_w + \mathbf{u}_o,$$
$$\mathbf{u}_{es} = \mathbf{G}^+\left(\frac{\partial H}{\partial \mathbf{q}} - \mathbf{M}\mathbf{M}_d^{-1}\frac{\partial H_d}{\partial \mathbf{q}}\right)$$
$$\mathbf{u}_{di} = -\mathbf{K}_v \mathbf{G}^T \mathbf{M}^{-T} \mathbf{M}_d^T \frac{\partial H_d}{\partial \bar{\mathbf{p}}} \tag{29}$$
$$\mathbf{u}_w = \mathbf{G}^+\mathbf{M}\mathbf{M}_d^{-1}(\mathbf{I} - \mathbf{M}_d\mathbf{M}^{-1})\mathbf{w}_{ext},$$

brings the system described in (10) into (28), which has desired 'apparent' physical properties.

The control loop providing $\mathbf{u}_i$ can be considered as a *low-level* one, which is responsible of controlling the APhI, and also accepts a *high-level* control input, $\mathbf{u}_o \in \mathbb{R}^4$, which can be computed for, e.g., position or force/torque tracking.

Proposition 2. *The controlled system (28) is cyclo-passive with respect to the input-output pair:*

$$\left\langle \begin{bmatrix} \mathbf{u}_o \\ \tilde{\mathbf{w}}_{ext} \end{bmatrix}, \begin{bmatrix} \mathbf{G}^T \mathbf{M}^{-T} \mathbf{M}_d^T \frac{\partial H_d}{\partial \bar{\mathbf{p}}} \\ \frac{\partial H_d}{\partial \bar{\mathbf{p}}} \end{bmatrix} \right\rangle.$$

Proof. Consider the energy function defined in (16). Using (28) we obtain:

$$\dot{H}_d = \begin{bmatrix} \frac{\partial^T H_d}{\partial \mathbf{q}} & \frac{\partial^T H_d}{\partial \bar{\mathbf{p}}} \end{bmatrix} \begin{bmatrix} \dot{\mathbf{q}} \\ \dot{\bar{\mathbf{p}}} \end{bmatrix}$$
$$= -\frac{\partial^T H_d}{\partial \bar{\mathbf{p}}} \mathcal{R}_d \frac{\partial H_d}{\partial \bar{\mathbf{p}}} + \frac{\partial^T H_d}{\partial \bar{\mathbf{p}}} \mathbf{M}_d\mathbf{M}^{-1}\mathbf{G}\mathbf{u}_o \tag{30}$$
$$+ \frac{\partial^T H_d}{\partial \bar{\mathbf{p}}} \tilde{\mathbf{w}}_{ext}.$$

Considering that $\mathcal{R}_d \geq \mathbf{0}$ by taking Remark 1 in to account, we obtain that

$$\dot{H}_d \leq \frac{\partial^T H_d}{\partial \bar{\mathbf{p}}} \mathbf{M}_d\mathbf{M}^{-1}\mathbf{G}\mathbf{u}_o + \frac{\partial^T H_d}{\partial \bar{\mathbf{p}}} \tilde{\mathbf{w}}_{ext} \tag{31}$$

which proofs the statement. ∎

2.4   Robustness of IDA-PBC

In this Section we provide a robustness analysis of the IDA-PBC strategy presented above (considering the $\mathbf{u}_i$ as computed in (29)) against noisy measurements[4]. Remember that this controller consists of three steps; *i)* energy shaping, *ii)* damping injection, *iii)* external wrench compensation. Our goal will be keeping the analysis simple and isolating the effects of disturbances on the single components of the control action. Let us consider the PH formalization of the system, which is not yet damped, and in which no external wrench is apparent:

$$\begin{bmatrix} \dot{\mathbf{q}} \\ \dot{\mathbf{p}} \end{bmatrix} = \begin{bmatrix} \mathbf{0} & \mathbf{I} \\ -\mathbf{I} & \mathbf{0} \end{bmatrix} \begin{bmatrix} \frac{\partial H}{\partial \mathbf{q}} \\ \frac{\partial H}{\partial \mathbf{p}} \end{bmatrix} + \begin{bmatrix} \mathbf{0} \\ \mathbf{G} \end{bmatrix} \mathbf{u}_{es}, \qquad (32)$$

where

$$\mathbf{G} = \begin{bmatrix} -\mathbf{R}(\boldsymbol{\eta})\mathbf{e}_3 & \mathbf{0} \\ \mathbf{0} & \mathbf{I} \end{bmatrix}, \quad \mathbf{G}^+ = \begin{bmatrix} -\mathbf{e}_3^T\mathbf{R}^T(\boldsymbol{\eta}) & \mathbf{0} \\ \mathbf{0} & \mathbf{I} \end{bmatrix}, \quad (33)$$

with $\mathbf{G}^+ = (\mathbf{G}^T\mathbf{G})^{-1}\mathbf{G}^T$. Consider the noisy states, which are used for computing the control inputs:

$$\begin{aligned} \tilde{\mathbf{q}} &= \begin{bmatrix} \tilde{\mathbf{p}}_q \\ \tilde{\boldsymbol{\eta}} \end{bmatrix} = \begin{bmatrix} \mathbf{p}_q \\ \boldsymbol{\eta} \end{bmatrix} + \begin{bmatrix} \mathbf{p}_{q_N} \\ \boldsymbol{\eta}_N \end{bmatrix} \\ \dot{\tilde{\mathbf{q}}} &= \begin{bmatrix} \dot{\tilde{\mathbf{p}}}_q \\ \dot{\tilde{\boldsymbol{\eta}}} \end{bmatrix} = \begin{bmatrix} \dot{\mathbf{p}}_q \\ \dot{\boldsymbol{\eta}} \end{bmatrix} + \begin{bmatrix} \dot{\mathbf{p}}_{q_N} \\ \dot{\boldsymbol{\eta}}_N \end{bmatrix}, \end{aligned} \qquad (34)$$

where $\tilde{\mathbf{q}}$ and $\dot{\tilde{\mathbf{q}}}$ indicate the noisy measurements of the configuration and of the velocity of the quadrotor CoM. Furthermore, the terms $\mathbf{p}_{q_N}$, $\boldsymbol{\eta}_N$, $\dot{\mathbf{p}}_{q_N}$ and $\dot{\boldsymbol{\eta}}_N$ indicate the bounded noises/disturbances affecting the measurements.

2.4.1   Energy shaping analysis: For now, consider only the energy shaping control input $\mathbf{u}_{es}$ as given in (20), which can be re-formalized as

$$\mathbf{u}_{es} = \mathbf{G}^+(\boldsymbol{\eta}) \left(\begin{bmatrix} \boldsymbol{\gamma} \\ \mathbf{0} \end{bmatrix} - \mathbf{M}\mathbf{M}_d^{-1} \begin{bmatrix} \boldsymbol{\gamma}_d \\ \nabla_{\boldsymbol{\eta}} V_d(\boldsymbol{\eta}) \end{bmatrix} \right), \qquad (35)$$

where $\boldsymbol{\gamma} = [0\ 0\ -mg]^T \in \mathbb{R}^3$, $\boldsymbol{\gamma}_d = [0\ 0\ -m_dg]^T \in \mathbb{R}^3$, and $\nabla_* f$ stands for $\frac{\partial f}{\partial *}$.

Considering the noises in the measurements, the noisy control input becomes

$$\tilde{\mathbf{u}}_{es} = \mathbf{G}^+(\tilde{\boldsymbol{\eta}}) \left(\begin{bmatrix} \boldsymbol{\gamma} \\ \mathbf{0} \end{bmatrix} - \mathbf{M}\mathbf{M}_d^{-1} \begin{bmatrix} \boldsymbol{\gamma}_d \\ \nabla_{\tilde{\boldsymbol{\eta}}} V_d(\tilde{\boldsymbol{\eta}}) \end{bmatrix} \right). \qquad (36)$$

Now, considering the last three rows of (32), we can write

$$\dot{\mathbf{p}} = -\nabla_{\mathbf{q}} H(\boldsymbol{\eta}) + \mathbf{G}(\boldsymbol{\eta})\mathbf{u}_{es} = -\begin{bmatrix} \boldsymbol{\gamma} \\ \mathbf{0} \end{bmatrix} + \mathbf{G}(\boldsymbol{\eta})\mathbf{u}_{es}. \quad (37)$$

Then, the way $\tilde{\mathbf{u}}_{es}$ affect the system in (32) is

$$\begin{aligned} \dot{\mathbf{p}} &= -\begin{bmatrix} \boldsymbol{\gamma} \\ \mathbf{0} \end{bmatrix} + \mathbf{G}(\boldsymbol{\eta})\tilde{\mathbf{u}}_{es} \\ &= -\begin{bmatrix} \boldsymbol{\gamma} \\ \mathbf{0} \end{bmatrix} + \mathbf{G}(\boldsymbol{\eta})\mathbf{u}_{es} + \mathbf{G}(\boldsymbol{\eta})(\tilde{\mathbf{u}}_{es} - \mathbf{u}_{es}). \end{aligned} \qquad (38)$$

Let us compute the explicit expression of the term $\mathbf{G}(\boldsymbol{\eta})\mathbf{u}_{es}$. Considering (35) together with (33), we can say

$$\begin{aligned} \mathbf{G}(\boldsymbol{\eta})\mathbf{u}_{es} &= \mathbf{G}(\boldsymbol{\eta})\mathbf{G}^+(\boldsymbol{\eta}) \left(\begin{bmatrix} \boldsymbol{\gamma} \\ \mathbf{0} \end{bmatrix} - \mathbf{M}\mathbf{M}_d^{-1} \begin{bmatrix} \boldsymbol{\gamma}_d \\ \nabla_{\boldsymbol{\eta}} V_d(\boldsymbol{\eta}) \end{bmatrix} \right) \\ &= -\mathbf{G}(\boldsymbol{\eta})\mathbf{G}^+(\boldsymbol{\eta}) \begin{bmatrix} \mathbf{0} \\ \mathbf{N}^{-1}\nabla_{\boldsymbol{\eta}} V_d(\boldsymbol{\eta}) \end{bmatrix} \\ &= -\begin{bmatrix} \mathbf{0} \\ \mathbf{N}^{-1}\nabla_{\boldsymbol{\eta}} V_d(\boldsymbol{\eta}) \end{bmatrix}. \end{aligned} \qquad (39)$$

Thus, we can write (38) as

$$\dot{\mathbf{p}} = -\begin{bmatrix} \boldsymbol{\gamma} \\ \mathbf{0} \end{bmatrix} - \begin{bmatrix} \mathbf{0} \\ \mathbf{N}^{-1}\nabla_{\boldsymbol{\eta}} V_d(\boldsymbol{\eta}) \end{bmatrix} + \mathbf{G}(\boldsymbol{\eta})(\tilde{\mathbf{u}}_{es} - \mathbf{u}_{es}). \quad (40)$$

Energy shaping control input reshapes the physics of the system by not only by assigning a desired inertia but also by changing its state from $\mathbf{p} = \mathbf{M}\dot{\mathbf{q}}$ to $\bar{\mathbf{p}} = \mathbf{M}_d\dot{\mathbf{q}}$, which considering (40) leads to

$$\begin{aligned} \dot{\bar{\mathbf{p}}} &= \mathbf{M}_d\mathbf{M}^{-1}\dot{\mathbf{p}} \\ &= -\begin{bmatrix} \boldsymbol{\gamma}_d \\ \mathbf{0} \end{bmatrix} - \begin{bmatrix} \mathbf{0} \\ \nabla_{\boldsymbol{\eta}} V_d(\boldsymbol{\eta}) \end{bmatrix} + \underbrace{\mathbf{M}_d\mathbf{M}^{-1}\mathbf{G}(\boldsymbol{\eta})(\tilde{\mathbf{u}}_{es} - \mathbf{u}_{es})}_{\mathbf{w}_{es}}, \end{aligned} \qquad (41)$$

where $\mathbf{w}_{es}$ is the wrench due to the effect of the noisy state disturbance to the energy shaping control input. Recalling from (39) that

$$\begin{aligned} \mathbf{G}(\boldsymbol{\eta})\mathbf{u}_{es} &= -\begin{bmatrix} \mathbf{0} \\ \mathbf{N}^{-1}\nabla_{\boldsymbol{\eta}} V_d(\boldsymbol{\eta}) \end{bmatrix} \\ \mathbf{G}(\boldsymbol{\eta})\tilde{\mathbf{u}}_{es} &= -\begin{bmatrix} \mathbf{0} \\ \mathbf{N}^{-1}\nabla_{\tilde{\boldsymbol{\eta}}} V_d(\tilde{\boldsymbol{\eta}}) \end{bmatrix} \end{aligned}$$

and placing them in $\mathbf{w}_{es}$ shown in (41), we can explicitly compute the effect of the disturbance as

$$\begin{aligned} \mathbf{w}_{es} &= \mathbf{M}_d\mathbf{M}^{-1} \left(\begin{bmatrix} \mathbf{0} \\ \mathbf{N}^{-1}\nabla_{\boldsymbol{\eta}} V_d(\boldsymbol{\eta}) \end{bmatrix} - \begin{bmatrix} \mathbf{0} \\ \mathbf{N}^{-1}\nabla_{\tilde{\boldsymbol{\eta}}} V_d(\tilde{\boldsymbol{\eta}}) \end{bmatrix} \right) \\ &= \begin{bmatrix} \mathbf{0} \\ \nabla_{\boldsymbol{\eta}} V_d(\boldsymbol{\eta}) \end{bmatrix} - \begin{bmatrix} \mathbf{0} \\ \nabla_{\tilde{\boldsymbol{\eta}}} V_d(\tilde{\boldsymbol{\eta}}) \end{bmatrix}. \end{aligned} \qquad (42)$$

Now, for a desired energy in form of (21) and (22), we can say that $\nabla_{\boldsymbol{\eta}} V_d(\boldsymbol{\eta}) = \mathbf{K_p}\boldsymbol{\eta}$ and $\nabla_{\tilde{\boldsymbol{\eta}}} V_d(\tilde{\boldsymbol{\eta}}) = \mathbf{K_p}\tilde{\boldsymbol{\eta}}$. Also remembering from (34) that $\tilde{\boldsymbol{\eta}} = \boldsymbol{\eta} + \boldsymbol{\eta}_N$, we can write $\mathbf{w}_{es}$ in (42) as

$$\mathbf{w}_{es} = \begin{bmatrix} \mathbf{0} \\ -\mathbf{K}_p\boldsymbol{\eta}_N \end{bmatrix}. \qquad (43)$$

Thus, we can conclude that the effect of the noisy states on the energy shaping step is given by a bounded torque only and it does not generate disturbing forces for the translational dynamics.

2.4.2   Damping injection analysis: A similar analysis can be done for the damping injection. From (24) we have that

$$\begin{aligned} \mathbf{u}_{di} &= \mathbf{S}(\boldsymbol{\eta})\dot{\mathbf{q}}, \\ \mathbf{S}(\boldsymbol{\eta}) &= -\mathbf{K}_v\mathbf{G}^T(\boldsymbol{\eta})\mathbf{M}^{-T}\mathbf{M}_d^T \\ \mathbf{K}_V &= \begin{bmatrix} k_T & \mathbf{0} \\ \mathbf{0} & \mathbf{K}_R \end{bmatrix}, \end{aligned} \qquad (44)$$

where the explicit expression of $\mathbf{S}(\boldsymbol{\eta})$ is,

$$\mathbf{S}(\boldsymbol{\eta}) = - \begin{bmatrix} -k_T \frac{m_d}{m} \mathbf{e}_3^T \mathbf{R}^T(\boldsymbol{\eta}) & \mathbf{0} \\ \mathbf{0} & \mathbf{K}_R \mathbf{N}^T \end{bmatrix}. \quad (45)$$

Now, similar to Section 2.4.1, and also recalling (10), the way $\mathbf{u}_{di}$ affects the system dynamics $\dot{\mathbf{p}}$ is through $\mathbf{G}(\boldsymbol{\eta})\mathbf{u}_{di}$. It affects the *energy shaped system* dynamics $\dot{\bar{\mathbf{p}}}$ through $\mathbf{M}_d \mathbf{M}^{-1} \mathbf{G}(\boldsymbol{\eta})\mathbf{u}_{di}$. By proceeding as in the previous section, and considering the damping injection control input computed using the noisy states, i.e., $\tilde{\mathbf{u}}_{di}$, we can write

$$\mathbf{M}_d \mathbf{M}^{-1} \mathbf{G}(\boldsymbol{\eta})\tilde{\mathbf{u}}_{di} = \mathbf{M}_d \mathbf{M}^{-1} \mathbf{G}(\boldsymbol{\eta})\mathbf{S}(\tilde{\boldsymbol{\eta}})\dot{\tilde{\mathbf{q}}}$$
$$= \mathbf{M}_d \mathbf{M}^{-1} \mathbf{G}(\boldsymbol{\eta})\Big(\mathbf{S}(\boldsymbol{\eta})\dot{\mathbf{q}} + \big(\mathbf{S}(\tilde{\boldsymbol{\eta}})\dot{\tilde{\mathbf{q}}} - \mathbf{S}(\boldsymbol{\eta})\dot{\mathbf{q}}\big)\Big), \quad (46)$$

from which we can see that the wrench generated by the state noises in the damping injection control input is

$$\mathbf{w}_{di} = \mathbf{M}_d \mathbf{M}^{-1} \mathbf{G}(\boldsymbol{\eta})\Big(\mathbf{S}(\tilde{\boldsymbol{\eta}})\dot{\tilde{\mathbf{q}}} - \mathbf{S}(\boldsymbol{\eta})\dot{\mathbf{q}}\Big). \quad (47)$$

After straightforward computations we can show that this wrench is in the form of

$$\mathbf{w}_{di} = - \begin{bmatrix} k_T \frac{m_d^2}{m^2} \mathbf{R}(\boldsymbol{\eta})\mathbf{e}_3\mathbf{e}_3^T \Big(\mathbf{R}^T(\tilde{\boldsymbol{\eta}})\dot{\bar{\mathbf{p}}}_q - \mathbf{R}^T(\boldsymbol{\eta})\dot{\mathbf{p}}_q\Big) \\ \mathbf{N}\mathbf{K}_R \mathbf{N}^T \dot{\boldsymbol{\eta}}_N \end{bmatrix}. \quad (48)$$

Thus, $\mathbf{w}_{di}$ is given by a bounded torque and by a force. Since toques are fully actuated, the torque disturbances are counter-actuated by the elastic potential and their effect is only to change the equilibrium point. Forces are more dangerous, since there may act along the underactuated directions ($\mathbf{x}$ and $\mathbf{y}$). However, notice that these forces vanishes with a decreasing damping parameter k_T, which is as expected from any damping-based control action. In case of high noise magnitudes that might lead destabilizing disturbance forces, a simple straightforward (and practical) solution may be reducing the damping gain $k_T \to 0$. In this way we do not inject additional damping on the translational direction and we keep only the aerodynamic damping that is acting on all directions, i.e., the system is still cyclo-passive.

2.4.3 Wrench compensation analysis: From (27) the control input for external wrench compensation is

$$\mathbf{u}_w = \mathbf{K}(\boldsymbol{\eta})\mathbf{w}_{ext}$$
$$\mathbf{K}(\boldsymbol{\eta}) = \mathbf{G}^+(\boldsymbol{\eta})\mathbf{M}\mathbf{M}_d^{-1}(\mathbf{I} - \mathbf{M}_d\mathbf{M}^{-1}), \quad (49)$$

which, as the others before, enters to the original system dynamics as $\mathbf{G}(\boldsymbol{\eta})\mathbf{u}_w$, and to the desired (target) system dynamics as $\mathbf{M}_d \mathbf{M}^{-1} \mathbf{G}(\boldsymbol{\eta})\mathbf{u}_w$.

Although we will follow the same procedure as before, notice that this time there could be two means of the noise disturbance affecting the control input[5]; either on $\boldsymbol{\eta}$ or $\mathbf{w}_{ext}$. This in mind, the noisy control input $\tilde{\mathbf{u}}_w$ enters the desired system dynamics as

$$\mathbf{M}_d \mathbf{M}^{-1} \mathbf{G}(\boldsymbol{\eta})\tilde{\mathbf{u}}_w = \mathbf{M}_d \mathbf{M}^{-1} \mathbf{G}(\boldsymbol{\eta})\mathbf{K}(\tilde{\boldsymbol{\eta}})\tilde{\mathbf{w}}_{ext}, \quad (50)$$

where

$$\tilde{\mathbf{w}}_{ext} = \mathbf{w}_{ext} + \mathbf{w}_{ext_N} = \begin{bmatrix} \mathbf{f}_{ext} \\ \boldsymbol{\tau}_{ext} \end{bmatrix} + \begin{bmatrix} \mathbf{f}_{ext_N} \\ \boldsymbol{\tau}_{ext_N} \end{bmatrix} \quad (51)$$

indicates the noisy wrench measurement with $\mathbf{w}_{ext_N} \in \mathbb{R}^6$ is the bounded noise/disturbance affecting this measurement. Then, following the same procedure as in the previous section, we can find the wrench appearing due to the noises in the wrench compensating control inputs as

$$\mathbf{w}_{co} = \mathbf{M}_d \mathbf{M}^{-1} \mathbf{G}(\boldsymbol{\eta})\Big(\mathbf{K}(\tilde{\boldsymbol{\eta}})\tilde{\mathbf{w}}_{ext} - \mathbf{K}(\boldsymbol{\eta})\mathbf{w}_{ext}\Big). \quad (52)$$

Now, let's analyze this wrench in different cases;

- Noise only on $\mathbf{w}_{ext}$

$$\mathbf{w}_{co} = \mathbf{M}_d \mathbf{M}^{-1} \mathbf{G}(\boldsymbol{\eta})\mathbf{K}(\boldsymbol{\eta})(\tilde{\mathbf{w}}_{ext} - \mathbf{w}_{ext})$$
$$= \begin{bmatrix} \mathbf{R}(\boldsymbol{\eta})\mathbf{e}_3\mathbf{e}_3^T\mathbf{R}^T(\boldsymbol{\eta})\mathbf{D} & \mathbf{0} \\ \mathbf{0} & (\mathbf{I} - \mathbf{N}) \end{bmatrix} \mathbf{w}_{ext_N} \quad (53)$$

- Noise only on $\boldsymbol{\eta}$

$$\mathbf{w}_{co} = \mathbf{M}_d \mathbf{M}^{-1} \mathbf{G}(\boldsymbol{\eta})\Big(\mathbf{K}(\tilde{\boldsymbol{\eta}}) - \mathbf{K}(\boldsymbol{\eta})\Big)\mathbf{w}_{ext}$$
$$= \begin{bmatrix} \mathbf{R}(\boldsymbol{\eta})\mathbf{e}_3\mathbf{e}_3^T\Big(\mathbf{R}^T(\tilde{\boldsymbol{\eta}}) - \mathbf{R}^T(\boldsymbol{\eta})\Big)\mathbf{D} & \mathbf{0} \\ \mathbf{0} & \mathbf{0} \end{bmatrix} \mathbf{w}_{ext} \quad (54)$$

- Noise only on both $\mathbf{w}_{ext}$ and $\boldsymbol{\eta}$

$$\mathbf{w}_{co} = \mathbf{M}_d \mathbf{M}^{-1} \mathbf{G}(\boldsymbol{\eta})\Big(\mathbf{K}(\tilde{\boldsymbol{\eta}}) - \mathbf{K}(\boldsymbol{\eta})\Big)(\tilde{\mathbf{w}}_{ext} - \mathbf{w}_{ext})$$
$$= \begin{bmatrix} \mathbf{R}(\boldsymbol{\eta})\mathbf{e}_3\mathbf{e}_3^T\mathbf{R}^T(\tilde{\boldsymbol{\eta}})\mathbf{D} & \mathbf{0} \\ \mathbf{0} & (\mathbf{I} - \mathbf{N}) \end{bmatrix} \tilde{\mathbf{w}}_{ext}$$
$$- \begin{bmatrix} \mathbf{R}(\boldsymbol{\eta})\mathbf{e}_3\mathbf{e}_3^T\mathbf{R}^T(\boldsymbol{\eta})\mathbf{D} & \mathbf{0} \\ \mathbf{0} & (\mathbf{I} - \mathbf{N}) \end{bmatrix} \mathbf{w}_{ext}$$
$$= \begin{bmatrix} \mathbf{R}(\boldsymbol{\eta})\mathbf{e}_3\mathbf{e}_3^T\Big(\mathbf{R}^T(\tilde{\boldsymbol{\eta}}) - \mathbf{R}^T(\boldsymbol{\eta})\Big)\mathbf{D}\mathbf{f}_{ext_N} \\ (\mathbf{I} - \mathbf{N})\boldsymbol{\tau}_{ext_N} \end{bmatrix} \quad (55)$$

where $\mathbf{D} = \mathbf{I}\frac{m - m_d}{m}$.

Notice that the effect of the measurement noises on the external wrench compensating control input along the fully actuated directions (rotational) are either bounded (which can always be counteracted), or they never appear. On the other hand the disturbing forces due to the measurement noises along the underactuated directions can be dangerous, which in each scenario can be canceled when setting $m_d = m \implies \mathbf{D} = \mathbf{0}$.

In summary, dividing the IDA-PBC control input into its components explicitly shows, which part of it is more problematic in terms of robustness against the noises (or inaccuracy) on the measurements. The energy shaping input $\mathbf{u}_{es}$ is not affected by the noises along the underactuated directions, and for the actuated directions the effect of noise is bounded. The damping injection control input is affected by the noises along the underactuated directions, which is harder to deal with (it is also affected by the noises along the actuated directions, but their effect only disturbs the system around its equilibrium which can always be counteracted). However by choosing $k_T \to 0$, one can avoid the wrenches caused by the noise. Similarly, the external wrench compensating control input is also affected by the

noises, and it is again not trivial to compensate the disturbing forces along the underactuated directions. One idea might be setting $m_d = m \implies \mathbf{D} = \mathbf{0}$, which removes the effects of the noises along the underactuated directions, however this would be a conservative action since in this case one cannot assign a desired mass to the quadrotor.

Notice that the high-level external control input $\mathbf{u}_o$ is still free to use for dealing with the effects of the measurement noises, which is a potential field of study in the scope of our future works.

Remark 2. *Here we presented a robustness analysis of the control input $\mathbf{u}_i$ against the noisy state and wrench measurements. To this end, notice that both the controller presented in Section 2.3 and the external wrench estimation (to be presented in Section 3.1) are done for the CoM of the system, namely the dynamics representing the motion of point $\mathrm{P_B}$, that is the center of the quadrotor body-fixed frame. Although the physical interaction considered in this paper is always through an interaction tool (see Fig. 3), its impact on the CoM dynamics is a matter of kinematics (with negligible tool mass) and subject to the rigid body transformations, as also studied in Sec. 3.2.*

Remark 3. *We note that quantitative analysis on the robustness of the proposed controller to parametric uncertainties (e.g., mass, moment of inertia) is in the scope of our future works. Moreover considering the dynamics of the interaction tool and controlling the tool-tip dynamics instead of the CoM of the quadrotor is another direction that extends the results of this paper.*

3   External Wrench: Estimation vs Measurement

For achieving a meaningful control of APhI, the external wrench knowledge is essential. Here we discuss two methods; indirect (estimation) and direct (measurement). Each method can overcome the other for different reasons. By estimating the external wrench, one can avoid additional hardware cost and weight (and thus increase the duration of flight). Especially for miniature quadrotor VTOLs, the load capacity is quite limited and they are not suited for carrying a heavy F/T transducer and its electronics. Moreover, an estimator can be developed for any point on the flying robot, while the information provided by the transducer is limited to its location[6].

On the other hand, F/T sensors provide typically more reliable measurements which are not affected by any modeling or estimation error. While an estimator must rely on the measurements of the other sensors, e.g., camera or IMU, F/T sensors give accurate and independent measurements. Especially for outdoor implementations of the quadrotors, using F/T sensors can be indispensable, since in outdoor already the state estimation is a challenging problem.

In this Section we describe the external wrenche estimator proposed in Yüksel et al. (2014a). Then we provide a measurement method using a low-cost light-weight 6D F/T sensor placed onboard of a quadrotor. Finally we compare the results of these two methods in an experimental scenario, and promote the usage of the F/T sensors for APhI tasks.

3.1   External Wrench Estimation

Wrench estimation for flying robots has been studied by different robotics groups. In Augugliaro and DAndrea (2013) a *Kalman filter* is used to estimate the external force. A more general method is proposed in Ruggiero et al. (2014), where a residual *momentum-based* wrench estimator for quadrotors is presented. This method is further analyzed in Tomic and Haddadin (2014). In McKinnon and Schoellig (2016) an algorithm based on *unscented quaternion estimator* is used for estimating the external wrenches acting on a quadrotor body.

In Yüksel et al. (2014a) we had presented a *nonlinear Lyapunov-based* disturbance observer for estimating the external wrenches acting on a quadrotor. For that we have considered the Lagrange dynamics of the system as

$$\mathbf{w}_{ext} = \mathbf{B}(\mathbf{q})\ddot{\mathbf{q}} + \mathbf{C}(\mathbf{q},\dot{\mathbf{q}})\dot{\mathbf{q}} + \mathbf{g} - \mathbf{G}(\mathbf{q})\mathbf{u}, \qquad (56)$$

with

$$\mathbf{B}(\mathbf{q}) = \begin{bmatrix} m\mathbf{I} & * \\ \mathbf{0} & {}^{W}\mathbf{M}_{qr}(\boldsymbol{\eta}) \end{bmatrix} = \mathbf{B}^{T} \in \mathbb{R}^{6\times6},$$

$$\mathbf{G}(\mathbf{q}) = \begin{bmatrix} -\mathbf{R}(\boldsymbol{\eta})\mathbf{e}_3 & \mathbf{0} \\ \mathbf{0} & \mathbf{I} \end{bmatrix} \in \mathbb{R}^{6\times4} \qquad (57)$$

$$\mathbf{C}(\mathbf{q},\dot{\mathbf{q}}) = \begin{bmatrix} \mathbf{0} & \mathbf{0} \\ \mathbf{0} & \mathbf{C}_r(\boldsymbol{\eta},\dot{\boldsymbol{\eta}}) \end{bmatrix} \in \mathbb{R}^{6\times6}, \; \mathbf{g} = \begin{bmatrix} -mg\mathbf{e}_3 \\ \mathbf{0} \end{bmatrix},$$

where ${}^{W}\mathbf{M}_{qr}(\boldsymbol{\eta}) = \mathbf{T}(\boldsymbol{\eta})^T \mathbf{M}_{qr}\mathbf{T}(\boldsymbol{\eta}) \in \mathbb{R}^{3\times3}$ is the rotational inertia matrix w.r.t $\mathcal{F}_W$ and $\mathbf{C}_r(\boldsymbol{\eta},\dot{\boldsymbol{\eta}}) \in \mathbb{R}^{3\times3}$ is the matrix representing the Coriolis terms for the rotational dynamics. See more details in Yüksel et al. (2014a) and Yüksel (2017).

It has been shown in Chen et al. (2000) and Nikoobin and Haghighi (2009) that for a similar model (serial manipulator arm), the following disturbance observer can be proposed

$$\begin{aligned} \dot{\hat{\mathbf{w}}}_{ext} &= \mathbf{L}(\mathbf{q},\dot{\mathbf{q}})(\mathbf{w}_{ext} - \hat{\mathbf{w}}_{ext}) = -\mathbf{L}(\mathbf{q},\dot{\mathbf{q}})\hat{\mathbf{w}}_{ext} \\ &\quad + \mathbf{L}(\mathbf{q},\dot{\mathbf{q}})\Big(\mathbf{B}(\mathbf{q})\ddot{\mathbf{q}} + \mathbf{C}(\mathbf{q},\dot{\mathbf{q}})\dot{\mathbf{q}} + \mathbf{g} - \mathbf{G}(\mathbf{q})\mathbf{u} \Big), \end{aligned}$$
$$(58)$$

where $\hat{\mathbf{w}}_{ext} = [\hat{\mathbf{f}}_{ext}^T \; \hat{\boldsymbol{\tau}}_{ext}^T]^T \in \mathbb{R}^6$ is the estimated wrench and $\mathbf{L}(\mathbf{q},\dot{\mathbf{q}}) \in \mathbb{R}^{6\times6}$ will be designed in order to ensure the convergence of the observer. Notice that we do not have any specific model of the external disturbance, hence we assume $\dot{\mathbf{w}}_{ext} = \mathbf{0}$. Then the observer error and its dynamics are:

$$\begin{aligned} \mathbf{e}_o &= \mathbf{w}_{ext} - \hat{\mathbf{w}}_{ext} \\ \dot{\mathbf{e}}_o &= \dot{\mathbf{w}}_{ext} - \dot{\hat{\mathbf{w}}}_{ext} = \mathbf{L}(\mathbf{q},\dot{\mathbf{q}})\hat{\mathbf{w}}_{ext} - \mathbf{L}(\mathbf{q},\dot{\mathbf{q}})\mathbf{w}_{ext}, \end{aligned}$$
$$(59)$$

which can be expressed as

$$\dot{\mathbf{e}}_o + \mathbf{L}(\mathbf{q}_q,\dot{\mathbf{q}}_q)\mathbf{e}_o = \mathbf{0}. \qquad (60)$$

This means that the choice of $\mathbf{L}(\mathbf{q},\dot{\mathbf{q}})$ will directly affect the asymptotic stability of the error dynamics.

Notice that in order to implement (58) one needs the knowledge of $\dot{\mathbf{q}}$, $\dot{\mathbf{q}}$, and $\ddot{\mathbf{q}}$, where for many platforms acceleration measurements might not be reliable, or even not available (e.g., for quadrotors the angular accelerations are not available for the common platforms). For this purpose

we define the auxiliary vector:

$$\boldsymbol{\Psi} = \hat{\mathbf{w}}_{ext} - \boldsymbol{\gamma}(\dot{\mathbf{q}}). \tag{61}$$

Now, by taking the time derivative of (61) and equating it to (58), and choosing

$$\frac{\partial \boldsymbol{\gamma}(\dot{\mathbf{q}})}{\partial \dot{\mathbf{q}}} = \mathbf{L}(\mathbf{q}, \dot{\mathbf{q}})\mathbf{B}(\mathbf{q}), \tag{62}$$

we can find the dynamics of the nonlinear observer as

$$\dot{\boldsymbol{\Psi}} = -\mathbf{L}(\mathbf{q}, \dot{\mathbf{q}})\boldsymbol{\Psi} +$$
$$+ \mathbf{L}(\mathbf{q}, \dot{\mathbf{q}})\Big(\mathbf{C}(\mathbf{q}, \dot{\mathbf{q}})\dot{\mathbf{q}} + \mathbf{g} - \mathbf{G}(\mathbf{q})\mathbf{u} - \boldsymbol{\gamma}(\dot{\mathbf{q}})\Big) \tag{63}$$
$$\hat{\mathbf{w}}_{ext} = \boldsymbol{\Psi} + \boldsymbol{\gamma}(\dot{\mathbf{q}}).$$

As it is seen from (60), we must choose $\mathbf{L}(\mathbf{q}, \dot{\mathbf{q}})$ such a way that the error dynamics become asymptotically stable. Moreover, the decision made in (62) brings a strict dependency of $\mathbf{L}(\mathbf{q}, \dot{\mathbf{q}})$ on the choice of $\boldsymbol{\gamma}(\dot{\mathbf{q}})$. We make the following choice:

$$\boldsymbol{\gamma}(\dot{\mathbf{q}}_q) = c_o\dot{\mathbf{q}}_q$$
$$\mathbf{L}(\mathbf{q}, \dot{\mathbf{q}}) = c_o\mathbf{B}(\mathbf{q})^{-1}, \tag{64}$$

for $c_o > 0$ is the *observer gain*.

Proposition 3. *Consider the wrench estimator* (63) *and assume that the roll and pitch velocities are bounded, i.e.* $|\dot{\phi}| < \tilde{\phi}$ *and* $|\dot{\theta}| < \tilde{\theta}$, *where* $\tilde{\phi}, \tilde{\theta} \in \mathbb{R}^+$. *If* $\dot{\mathbf{w}}_{ext} = \mathbf{0}$ *holds and if* $\mathbf{L}(\mathbf{q}, \dot{\mathbf{q}})$ *is defined as in* (64), *then it is possible to have* $\hat{\mathbf{w}}_{ext} \to \mathbf{w}_{ext}$.

Proof. We will provide here a sketch of proof, more details can be found in Yüksel et al. (2014a). To do so, we will show that the estimation error defined in (59) will asymptotically vanish because the error dynamics (60) is asymptotically stable at $\mathbf{e} = \mathbf{0}$. Let

$$V(\mathbf{e}_o, \mathbf{q}) = \mathbf{e}_o^T\mathbf{B}(\mathbf{q})\mathbf{e}_o \tag{65}$$

be a positive definite candidate Lyapunov function. Considering (60) and (62), we can write:

$$\dot{V} = 2\mathbf{e}_o^T\mathbf{B}\dot{\mathbf{e}}_o + \mathbf{e}_o^T\dot{\mathbf{B}}\mathbf{e}_o =$$
$$= -2\mathbf{e}_o^T\mathbf{B}\mathbf{L}\mathbf{e}_o + \mathbf{e}_o^T\dot{\mathbf{B}}\mathbf{e}_o = -2c_o\mathbf{e}_o^T\mathbf{e}_o + \mathbf{e}_o^T\dot{\mathbf{B}}\mathbf{e}_o. \tag{66}$$

The first component of the right hand side of (66) is negative definite for $c_o \in \mathbb{R}^+$. The second component has an indefinite sign. Nevertheless, since $\mathbf{B}(\mathbf{q}) = \mathbf{B}^T(\mathbf{q})$, $\dot{\mathbf{B}}(\mathbf{q}, \dot{\mathbf{q}})$ is symmetric and, therefore, its eigenvalues are real. Since $|\dot{\phi}| < \tilde{\phi}$ and $|\dot{\theta}| < \tilde{\theta}$, from Yüksel et al. (2014a) and Yüksel (2017), it is easy to find two finite numbers $\alpha, \beta \in \mathbb{R}$ such that $\alpha < \dot{B}_{ij} < \beta$, $i, j \in \{1, \dots, 6\}$, where $\dot{B}_{ij}$ is the ij-th element of $\dot{\mathbf{B}}$. Thus, as shown in Zhan (2006), it is always possible to find a finite upper bound λ_B for all the possible eigenvalues of $\dot{\mathbf{B}}(\mathbf{q}_q, \dot{\mathbf{q}}_q)$:

$$\max_{\mathbf{q}, \dot{\mathbf{q}}} \lambda_M\left\{\dot{\mathbf{B}}(\mathbf{q}, \dot{\mathbf{q}})\right\} \leq \lambda_B < \infty, \tag{67}$$

where $\lambda_M\left\{\dot{\mathbf{B}}(\mathbf{q}, \dot{\mathbf{q}}_q)\right\}$ is the maximum eigenvalue of $\dot{\mathbf{B}}(\mathbf{q}, \dot{\mathbf{q}})$. Thus, we have that

$$\mathbf{e}_o^T\dot{\mathbf{B}}\mathbf{e}_o \leq \lambda_B\mathbf{e}_o^T\mathbf{e}_o. \tag{68}$$
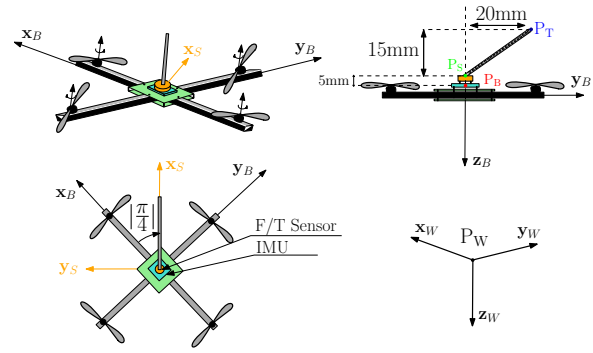

Figure 3. Placement of the interaction tooltip on top of the quadrotor: IMU (turquoise), Force/Torque sensor (orange) and the rigid tool (gray) and its tip (blue). This setup is later realized both as CAD model and in reality as shown in Fig. 4. The distances shown here match with the real design.

It is therefore possible to choose a $c_o > \frac{\lambda_B}{2}$ which implies $\dot{V}$ is negative definite and that, therefore, $\mathbf{e}_o(t) \to \mathbf{0}$ which proves the statement. ∎

3.2 External Wrench Measurement

Measuring contact forces and torques is possible using F/T sensors, which are already in use for robotic manipulators and humanoids (see Siciliano and Khatib (2008)). Recently they have been in use also for the aerial robots. In Gioioso et al. (2014) it has been shown how to turn a quadrotor into a 3D force tool, and for the experimental setup an F/T sensor was used. In that work, like in many, the F/T sensor is either placed in the environment, e.g., mounted on a wall, or on the robot but only when it is not completely flying, i.e., when the robot is fixed to a test bench as in Yu and Ding (2012) and Schiano et al. (2014). One of the main reasons why these sensors are not yet used on board of a flying aerial vehicle, is because of their weight. Especially considering their electronics, e.g., the data acquisition box, most of the aerial robots used in research are not capable of flying with these sensors on board.

However, recently some light-weight 6D F/T sensors appeared on the market. For the experiments of this paper, we have decided to use the *FTSens* 6D F/T sensor, developed by the *Italian Institute of Technology* (IIT), as introduced in Fumagalli et al. (2012a). This sensor weights 0.122 [kg] including all the electronics and its costs is relatively low w.r.t its pairs in the market. All these factors make this sensor a suitable candidate to be used on board of an aerial robot. This paves the way of using them as direct measurement sources, which feed the wrench measurements back to the control algorithms (e.g., the one sketched in Fig. 2). The details of the hardware and software for the FTsens F/T sensor is given in Section 4.2, and the experimental setup consisting of a quadrotor equipped with this sensor is shown in Fig. 4. To our best knowledge, this is the first quadrotor setup in the literature, which can freely fly with a 6D F/T sensor and its all electronics onboard, and perform APhI tasks.

Now let us give the details of its usage on board of a quadrotor VTOL. A sketch of our quadrotor and the F/T sensor setup is given in Fig. 3. On top of the F/T sensor a
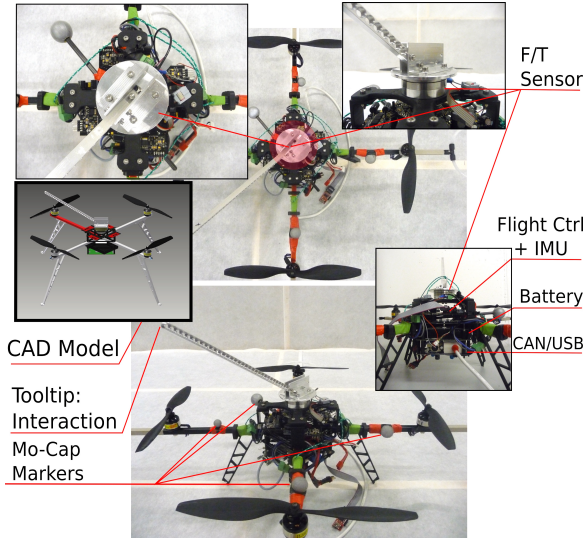
Figure 4. Quadrotor with F/T sensor (*FTSens*) on board. This is the experimental setup. Notice that the CAD model is developed based on the description in Fig. 3, and so is the real robot. Both the F/T sensor and the interaction tool are placed on top of the quadrotor. The hardware for the CAN-USB communication, is placed on the bottom of the robot. For this setup, it is $m = 1.49$ [kg], and $\mathbf{M}_{qr} = \text{diag}([0.01708, 0.0172, 0.0274]) \in \mathbb{R}^{3\times3}$ in units of [kgm²].

rigid tool is placed, intended to be used as the *interaction* tool with the environment (note that the mass of the manipulation tool is part of the overall quadrotor mass, but it is not considered separately for the controller.). We intentionally placed this rigid tool in a way, that there is $|\pi/4|$ [rad] between the tool tip and the quadrotor frame; so that the propellers will be away from the obstacles when the tool-tip is interacting with its environment. The CAD design of this setup is shown in Fig. 4, where we also present its realization in detail.

Unlike a model-based indirect estimation method, e.g., the one presented in Section 3.1, with using transducers our measurements are limited to the location of the sensor. Hence now our goal is to compute the external wrenches acting on different parts of the quadrotor, using the measurements acquired from the F/T sensor and rigid-body coordinate transformation methods. We had previously defined $\mathcal{F}_W : \{\mathrm{P}_W, \mathbf{x}_W, \mathbf{y}_W, \mathbf{z}_W\}$ as the world frame, and $\mathcal{F}_B : \{\mathrm{P}_B, \mathbf{x}_B, \mathbf{y}_B, \mathbf{z}_B\}$ is the body-fixed frame of the quadrotor. Now, let us define the $\mathcal{F}_S : \{\mathrm{P}_S, \mathbf{x}_S, \mathbf{y}_S, \mathbf{z}_S\}$ as the F/T sensor frame. Assume that the Inertial Measurement Unit (IMU) frame is same as $\mathcal{F}_B$. Then define $\mathcal{F}_{Sb} : \{\mathrm{P}_S, \mathbf{x}_{Sb}, \mathbf{y}_{Sb}, \mathbf{z}_{Sb}\}$ as the frame of the F/T sensor, after its orientation is aligned with the orientation of the body-fixed frame. Then let us define the following wrench informations:

- The external wrench acting at and about the tip point of the tool (P_T), is defined with $\mathbf{w}_t \in \mathbb{R}^6$ in $\mathcal{F}_W$, since the external forces and torques are coming from the world frame.

- The wrench measured by the sensor, is defined with $\tilde{\mathbf{w}}_s \in \mathbb{R}^6$ in $\mathcal{F}_S$, since the measurements are done in the sensor frame,

- The wrench measured by the sensor and adapted to the body frame, is defined with $\mathbf{w}_s \in \mathbb{R}^6$ in $\mathcal{F}_{Sb}$, since the sensor is fixed to the body of the quadrotor,

- The wrench entering to the quadrotor dynamics, is defined with $\mathbf{w}_{ext} \in \mathbb{R}^6$, where the forces are defined in $\mathcal{F}_W$ and the torques are in $\mathcal{F}_B$ so equivalently in $\mathcal{F}_{Sb}$. This is because of the choice made when writing the quadrotor equations of motion in Section 2.3, where the translational dynamics is written in the world frame, while the rotational one is in the body frame. Notice also that the controller developed in this paper accepts this wrench as an input (see also Fig. 2).

Now, it is clear that the only measurement we get is $\tilde{\mathbf{w}}_s \in \mathbb{R}^6$ in $\mathcal{F}_S$, but we need $\mathbf{w}_{ext} \in \mathbb{R}^6$ for the controller presented in Section 2.3, and maybe also $\mathbf{w}_t \in \mathbb{R}^6$ in $\mathcal{F}_W$ for visualization or for another type of controller. Then let us clarify the following relationship between the different wrench informations:

- Find $\mathbf{w}_s \in \mathbb{R}^6$ in $\mathcal{F}_{Sb}$. To do so, change the F/T sensor frame from $\mathcal{F}_S$ to $\mathcal{F}_{Sb}$. Notice that it can be done using time invariant rotations only (see Fig. 3 for the orientations of the frames). More specifically, remembering that $\mathcal{F}_S : \{\mathrm{P}_S, \mathbf{x}_S, \mathbf{y}_S, \mathbf{z}_S\}$ and $\mathcal{F}_{Sb} : \{\mathrm{P}_S, \mathbf{x}_{Sb}, \mathbf{y}_{Sb}, \mathbf{z}_{Sb}\}$, we have

$$\begin{bmatrix} \mathbf{x}_{Sb} \\ \mathbf{y}_{Sb} \\ \mathbf{z}_{Sb} \end{bmatrix} = \mathbf{R}_S^B \begin{bmatrix} \mathbf{x}_S \\ \mathbf{y}_S \\ \mathbf{z}_S \end{bmatrix}, \quad \mathbf{R}_S^B = \mathbf{R}_{x_S}(\pi)\mathbf{R}_{z_S}(\pi/4), \tag{69}$$

where $\mathbf{R}_{*_S}$ is the rotation matrix defined in $\mathcal{F}_S$ and around $*$-axis. Hence, if $\tilde{\mathbf{w}}_s \in \mathbb{R}^6$ is the measurement of the F/T sensor defined in $\mathcal{F}_S$ (because it is fixed in the sensor frame), then

$$\mathbf{w}_s = \begin{bmatrix} \mathbf{R}_S^B & \mathbf{0} \\ \mathbf{0} & \mathbf{R}_S^B \end{bmatrix} \tilde{\mathbf{w}}_s \tag{70}$$

is the measurement but defined[7] in $\mathcal{F}_{Sb}$. Notice that $\mathbf{R}_S^B$ is a constant (time invariant) matrix, and $\mathbf{0}$ is a matrix, which consists of only zeros.

- Find $\mathbf{w}_t \in \mathbb{R}^6$ in $\mathcal{F}_W$. To do so, let us use the recently computed $\mathbf{w}_s$. This can be done using the following relation:

$$\mathbf{w}_s = \begin{bmatrix} \mathbf{R}_W^B(\boldsymbol{\eta}) & \mathbf{0} \\ [\mathbf{d}_l]_\wedge \mathbf{R}_W^B(\boldsymbol{\eta}) & \mathbf{R}_W^B(\boldsymbol{\eta}) \end{bmatrix} \mathbf{w}_t, \tag{71}$$

where $\mathbf{R}_W^B(\boldsymbol{\eta})$ is the rotation matrix representing the orientation of $\mathcal{F}_W$ in $\mathcal{F}_B$, which is time variant due to the dependency of the quadrotor orientation $\boldsymbol{\eta} \in \mathbb{R}^3$. Notice that $\mathbf{d}_l \in \mathbb{R}^3$ is the distance between P_T and P_S in $\mathcal{F}_{Sb}$ frame[8], and $[\star]_\wedge : \mathbb{R}^3 \to so(3)$ is the skew-symmetric operator. Hence, using $\mathbf{w}_s$ from (70), we can compute $\mathbf{w}_t$ using the relation in (71).

- Find $\mathbf{w}_{ext} \in \mathbb{R}^6$. To do so, use the rigid transformation from $\mathbf{w}_s$ to $\mathbf{w}_{ext}$:

$$\mathbf{w}_{ext} = \begin{bmatrix} \mathbf{R}_B^W(\boldsymbol{\eta}) & \mathbf{0} \\ [\mathbf{d}_s]_\wedge \mathbf{R}_B^W(\boldsymbol{\eta}) & \mathbf{I} \end{bmatrix} \mathbf{w}_s, \tag{72}$$
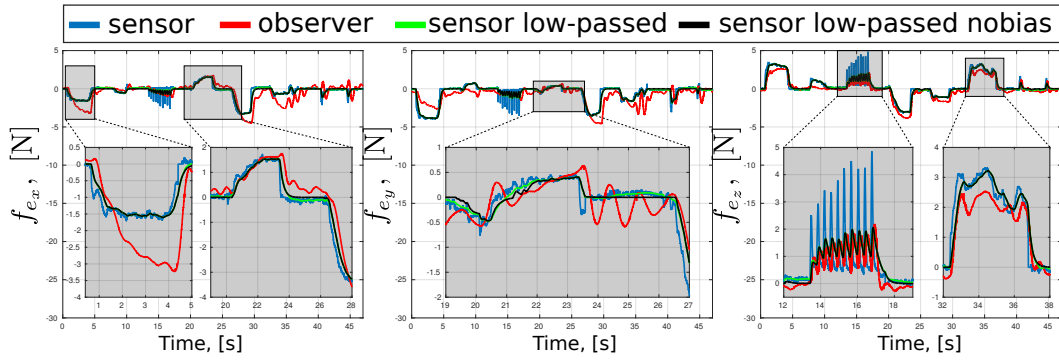
Figure 5. Comparison between the F/T sensor (see Section 3.2) and the observer (see Section 3.1). Only the measured/estimated forces are shown, in units of [N]. Raw sensor readings are depicted with blue curves, and the output of the observer is with red ones. Green color is used for the measured forces which are *low-pass filtered*. Black curves are used when the bias of this low-pass filtered data is removed in real time (which we used in our experiments in Section 4 when implementing the IDA-PBC method, with also considering the transformations explained in Section 3.2). The magnified plots of the each grayed box is placed close by, for better comparison of the different values.

where $\mathbf{R}_B^W(\boldsymbol{\eta})$ is the rotation matrix representing the orientation of $\mathcal{F}_B$ in $\mathcal{F}_W$, $\mathbf{I}$ is an identity matrix, and $\mathbf{d}_s$ is the distance between $\mathrm{P_S}$ and $\mathrm{P_B}$ in $\mathcal{F}_B$, which is $\mathbf{d}_s = [0\ 0\ -0.05]$ [m].

Hence, for finding the effect of $\mathbf{w}_t$ (defined in $\mathcal{F}_W$) to the body-fixed frame of the quadrotor (this effect is named as $\mathbf{w}_{ext}$ in our convention), one can first use the F/T sensor measurements $\tilde{\mathbf{w}}_s$ in $\mathcal{F}_S$, then compute $\mathbf{w}_s$ in $\mathcal{F}_{Sb}$, and then finally use (72). For finding what $\mathbf{w}_t$ exactly is, one can use (71).

Notice that when using the NED convention, the rotation matrix from body to the world frame is $\mathbf{R}_B^W(\boldsymbol{\eta}) = \mathbf{R}$ where $\mathbf{R} \in \mathrm{SO}(3)$ as mentioned in Section 2.3 and it is true that $\mathbf{R}_W^B(\boldsymbol{\eta}) = \mathbf{R}_B^{W^T}(\boldsymbol{\eta})$.

3.3 Comparison between Estimation and Direct Measurement

In Yüksel et al. (2014a) the numerical (simulative) results of the wrench estimation (Section 3.1) has been shown. There, decent wrench estimation performances have been achieved, even when the noises of the other measurements are taken into account. The performance of the proposed observer strongly relies on the choice of the observer gain (see Yüksel et al. (2014a)).

Although tuning this gain in the numerical simulations was relatively easy, for the real experiments it was hard to find a compromise between the convergence of the estimation and its performance, as it will be seen in the following comparison.

For the experimental setup, we used the aerial robot in Fig. 4, where the overall quadrotor is controlled using the IDA-PBC controller (explained in Section 2.3). We then implemented the nonlinear wrench observer (given in Section 3.1). For the experiment we have disturbed the hovering quadrotor by changing external forces and torques at the tip point of the rigid link (see Fig. 4), which is rigidly attached to the F/T sensor that is placed on board of the quadrotor (more details of the experimental setup is given in Section 4).

The online collected external force data are presented in Fig. 5, where the F/T sensor measurements (see sensor

details in Section 4.2) are compared with the wrench observer values[9]. The blue curves stand for the raw sensor measurements and the green curves are a low-pass filtered version of the blue ones. Further fining is done by removing the sensor bias online and the result is depicted with black curves. The observer data is shown with red. As it is seen from Fig. 5, the observer follows the sensor data (which one may consider also as the ground truth), but with some oscillations and even with some offset. This is mainly due to the poor tuning of the observer gain c_o, and partly due to the small imprecision of the mathematical model. Especially for f_{e_x} and f_{e_y}, the observer performs worse than the sensor data. However, notice that for f_{e_z}, the observer tracks the sensor data much better, because it is the direction where the aerial platform is fully actuated. Notice that although the model errors, e.g., imprecise mass of the system still causes some offsets, the overall estimation is less oscillatory compared to f_{e_x} and f_{e_y}.

We also note that different estimation methods, e.g., the one in McKinnon and Schoellig (2016), might perform better under certain conditions. However, it is noticeable that using an F/T sensor allows acquiring the exact wrench information, independent from any system model. Moreover, in this case the wrench information would not be corrupted by any other sensor measurement, e.g., the ones that provide the state of the robot (see IMU and Mocap in Section 4.1). There could be a case, in which the state of the robot might be miscalculated, which might not be crucial when the robot is in *free flight*, i.e., not in APhI, but in case of APhI this might bring instability if the wrench estimation is used in the controller. Such a case can occur more frequently, especially when the robot is performing an outdoor task, where accurate state estimation of the flying robot is already a great challenge considering different weather, light and environment conditions.

Consequently, using a low-cost, light weight F/T sensor could be a beneficial choice, providing robust and accurate measurements for the indoor and future outdoor experiments. For all these reasons, we choose to use the F/T sensor setup for our APhI experiments in this paper.

4 Experiments

The experiments are managed using a stationary PC with Linux 14.04 on it, which communicates with the experimental setup (robot in Fig.4) through serial channels. Besides the codes embedded on board of the quadrotor setup, all experiments are programmed in this PC in ROS-Indigo environment and *TeleKyb* framework: an open-source end-to-end ROS-based software for general purpose of mobile robot control developed at Max Planck Institute for Biological Cybernetics, Tübingen (for details, see Grabe et al. (2013)). Using a custom joystick high level decisions are indicated to the robot, e.g., hovering, trajectory assigning or landing.

The experimental setup consist of a quadrotor equipped with various sensors including F/T sensor on board. This sensor is connected to a rigid interaction tool (see Fig. 4). Let us describe the individual parts of this setup in the following.

4.1 Quadrotor

The main body of the quadrotor setup is manufactured by *HiSystems GmbH*, and named as *Mikrokopter* Quadrotor[10]. The overall setup (including the F/T sensor and its electronics) weights 1.49 [kg] and from its CAD model we computed its moment of inertia as $\mathbf{M}_{qr} = \text{diag}([0.01708, 0.0172, 0.0274]) \in \mathbb{R}^{3\times3}$ in units of $[\text{kgm}^2]$.

The quadrotor has four rigid bars, connecting four brushless motors (will be referred as BL-Motors or BLDC) and their propellers to the main body of the robot (see Fig. 4). Notice that propellers are rigidly attached to their motors, as well as the motors to the bars, and bars to the body. On top of them there are four brushless motor controllers (BL-CTRL), a flight controller with an *Inertial Measurement Unit* (IMU) on it and markers for a *Motion Capture* (MoCap) system, in this order. Below the rigid bars there is the battery as the energy source.

Each BL-CTRL has one ATMEGA168 μ-controller[11], which is connected via I^{2}C bus to a *flight controller* including an *Inertial Measurement Unit* (IMU). All brushless motor, hence propeller velocities, depicted with Ω_i in Fig. 1, are controlled using a *Motor Controller* developed at LAAS-CNRS[12] (see also Franchi and Mallet (2017)). Through a serial channel we communicate with the flight controller, allowing us to read/write data from/to both the flight controller and the brushless motor controllers.

For state estimation of the robot, we use an external MoCap system (with six near-infrared cameras) and an IMU on board of the quadrotor. The MoCap system provides the pose of the quadrotor, $\mathbf{q} = [\mathbf{p}_q^T, \boldsymbol{\eta}^T]^T \in \mathbb{R}^6$ in the world frame at 120 [Hz]; while the IMU is giving the linear acceleration, $\ddot{\mathbf{p}}_q \in \mathbb{R}^3$, in the world frame and the angular velocity of the body (in the body frame), $\boldsymbol{\omega} \in \mathbb{R}^3$, both at 1 [kHz]. However, for the controller in Section 2.3 and the wrench estimator in Section 3.1 we need the state of the quadrotor, i.e., $\mathbf{q}$ and $\dot{\mathbf{q}}$, which is computed using an *Unscented Kalman Filter* (UKF) developed at LAAS-CNRS[13]. This algorithm fuses both IMU and MoCap data and provides an estimate of the quadrotor state at 1 [kHz].

4.2 F/T Sensor

In our experiments we used the *FTSens* F/T sensor, produced by (Italian Institute of Technology) IIT originally for the
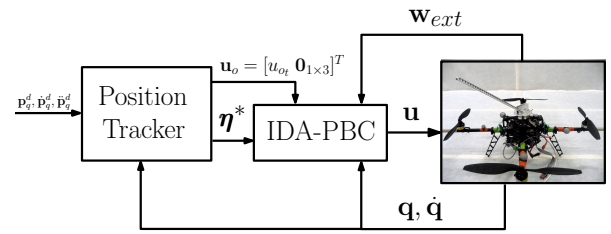

Figure 6. Sketch of the control framework used for the experiments. The position tracker is developed based on a position controller, sending the desired attitude equilibrium $\boldsymbol{\eta}^*$ and the high-level control input $\mathbf{u}_o$ to the IDA-PBC controller.

ICub humanoid robots (see Fumagalli et al. (2012a)). There are two reasons why we chose this sensor; first it was relatively cheaper than its peers in the market, and second it weights 0.122 [kg] together with its electronics. This is definitely in the load range of our quadrotor. The sensor is provided with proper calibrations by IIT for the measurement range of interest. A challenge of using this sensor was implementing the software for acquiring the meaningful force/torque measurements, from scratch. The FTSens communicates through the *Controller Area Network* (CAN) bus channel, in which it receives the commands and sends the sensor data based on the CAN protocol.

For this setup to work, both the computer and the sensor were needed to be programmed properly. The software package we have created for this sensor is available for the public use[14]. There we provide description and the source codes for:

- setting up your computer (for both Intel or ARM processors) for using the CAN-USB converter,

- getting the calibration data from the sensor and letting it send the raw data to the computer.

The details on the communication protocol of the sensor are available in the wiki-page of the ICub[15]. Using this *driver* it is possible to receive the *raw data* from the FTSens F/T sensor.

For processing this raw data, we implemented a ROS (C++) based software within the TeleKyb framework[16]. This software is tested with ROS-Indigo in Ubuntu 14.04 OS. It receives the raw data from the serial channel the sensor is connected to (through a CAN-USB converter) and as output returns the force and torque measurements in meaningful units as a ROS message. In this way the output can also be used by other ROS-based packages, e.g., the controller tested in Section 4.4 and Section 4.5. Notice that this code is strongly depended on both ROS and TeleKyb message types and their existing packages. Its usage for our experiments is also made available to the public[17], but for the initial access a permission from Max Planck Society would be needed.

4.3 Position Tracker

A high-level position tracker is used for steering the quadrotor VTOL to a desired trajectory, while letting IDA-PBC shape its physical properties. This tracking controller is developed based on a *position controller*, presented in Lee et al. (2013). From the decoupling property of the quadrotor, the rotational dynamics in (7) can be computed

independently from the translational dynamics given in (6). Let us consider a desired position trajectory of the quadrotor as $\mathbf{p}_q^d = [x_q^d \; y_q^d \; z_q^d]^T \in \mathbb{R}^3$, and assume that $\mathbf{f}_{ext} = \mathbf{0}$. Then, following from Lee et al. (2013), and from the third row of (6), the thrust input

$$u_{o_t} = -\frac{m_d}{c_\phi c_\theta}(g + \ddot{z}_q^d + k_{d_z}(\dot{z}_q^d - \dot{z}_q) + k_{p_z}(z_q^d - z_q)) \tag{73}$$

ensures the local exponential stability of $(z_q^d - z)$, as long as $c_\phi c_\theta \neq 0$, which is violated only when the quadrotor configuration is in a singularity that we avoid all the time. The control gains $k_{d_*} \in \mathbb{R}_{\geq 0}$ and $k_{p_*} \in \mathbb{R}_{\geq 0}$ are used for removing the velocity and position errors along the $*$-axes, respectively, where $* = \{\mathbf{x}, \mathbf{y}, \mathbf{z}\}$. From the first two rows of (6) we have

$$m_d \begin{bmatrix} \ddot{x}_q \\ \ddot{y}_q \end{bmatrix} = -u_{o_t} \underbrace{\begin{bmatrix} c_\phi c_\psi & s_\psi \\ c_\phi s_\psi & -c_\psi \end{bmatrix}}_{=:\mathbf{W}(\phi,\psi) \in \mathbb{R}^{2 \times 2}} \begin{bmatrix} s_\theta \\ s_\phi \end{bmatrix}, \tag{74}$$

where $\mathbf{W}$ is always invertible as long as $c_\phi \neq 0$; which means that the system is not in singularity. Then choosing the following roll and pitch commands will make $(x_q^d - x_q, \; y_q^d - y_q)$ locally exponentially stable

$$\begin{bmatrix} \bar{\theta}_c = s_{\theta^d} \\ \bar{\phi}_c = s_{\phi^d} \end{bmatrix} = $$
$$-\frac{m_d \mathbf{W}^{-1}}{u_{o_t}} \begin{bmatrix} \ddot{x}_q^d + k_{d_x}(\dot{x}_q^d - \dot{x}_q) + k_{p_x}(x_q^d - x_q) \\ \ddot{y}_q^d + k_{d_y}(\dot{y}_q^d - \dot{y}_q) + k_{p_y}(y_q^d - y_q) \end{bmatrix}. \tag{75}$$

In this step of the computations, let us define some maximum boundaries to both roll and pitch commands, preventing the system coming close to its singularities. In our experiments, we choose $\phi_c^{max} = \theta_c^{max} = \sin(r_l)$, where $r_l = 0.52326$ [rad]. Then let us implement the following soft saturation for both roll and pitch commands;

$$\phi_c = \frac{2\phi^{max}}{\pi} \arctan\left(\frac{\bar{\phi}_c}{2\phi_c^{max}}\right)$$
$$\theta_c = \frac{2\theta_c^{max}}{\pi} \arctan\left(\frac{\bar{\theta}_c}{2\theta_c^{max}}\right).$$

Then, the desired roll and pitch angles to steer the system to the desired $\mathbf{x}$ and $\mathbf{y}$ configurations are

$$\phi^* = \arctan(\phi_c), \quad \theta^* = \arctan(\theta_c). \tag{76}$$

Now, remember that in (22), we showed how one can change the desired attitude equilibrium $\boldsymbol{\eta}^* = [\phi^* \; \theta^* \; \psi^*]^T \in \mathbb{R}^3$, which shapes the desired potential energy of the system as, $V_d(\mathbf{q})$. Then using the desired attitude equilibrium ϕ^*, θ^* from (76), and ψ^* is chosen any arbitrary number, e.g., $\psi^* = 0$, and placing this desired potential energy $\bar{V}_d$ in (22) and ultimately using in $V_d(\mathbf{q})$; we make sure that the IDA-PBC controller can steer the system to a desired $\mathbf{x}_W - \mathbf{y}_W$ configuration using the control input in (29), with the desired physical behavior we have assigned to it. Moreover, by choosing the high-level control input as $\mathbf{u}_o = [u_{o_t} \; \mathbf{0}_{1 \times 3}]^T \in \mathbb{R}^4$, and implementing it in (29), we can let the quadrotor track a trajectory along the $\mathbf{z}_W$ axis with desired physical properties. A sketch of this control scheme is depicted in Fig. 6 for fixing the ideas.
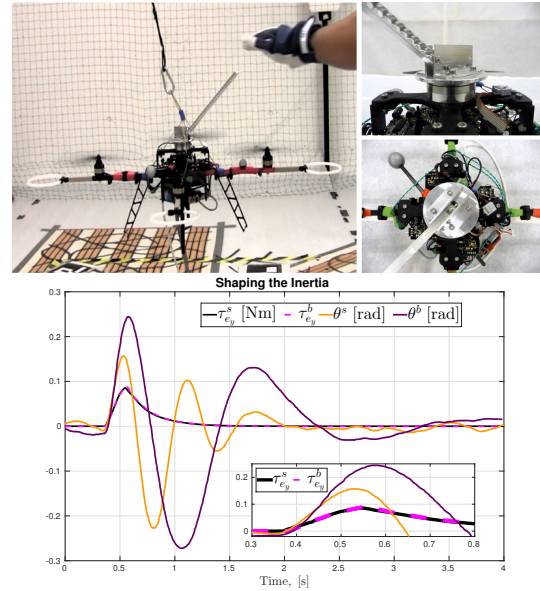

Figure 7. – *Top:* Quadrotor equipped with an F/T sensor (see details of the setup in Section 3.2) is about to be disturbed by an external interaction from the tip point of the rigid tool, during the hovering condition. For security reasons, a cable with no tension is connected to the system from the top.
– *Bottom:* System response (second order rotational dynamics) to the external disturbances around the $\mathbf{y}_B$ axis. Two cases are compared: system with bigger desired inertia (denoted with superscript $*^b$) and the one with smaller desired inertia (denoted with $*s$). Our proposed controller is used to assign the desired inertial properties, together with a high-level position controller described in Section 4.3.

Remark 4. *Notice, also from Fig. 6, that the high-level control input $\mathbf{u}_o$ is providing only the additional thrust input for tracking z_q^d and its derivatives. Other desired trajectories along the underactuated directions, i.e., $\mathbf{x}_W$ and $\mathbf{y}_W$, are tracked using solely the control inputs generated by IDA-PBC, i.e., $\mathbf{u}_i$. However to generate this input, we actively compute a new desired attitude $\boldsymbol{\eta}^*$, which is done using the near-hovering scheme presented in Section 4.3.*

4.4 Shaping the Inertia

As explained in Section 2.3, IDA-PBC is a powerful method for controlling the physical interaction of the quadrotor by shaping its physical properties, through passivation. To test this in real experiments, we first bring the quadrotor to a hovering condition using the controller depicted in Fig. 6. Then the flying system is disturbed with an external interaction on top of its tool tip, as shown in the top of Fig. 7. We repeat this twice; first the IDA-PBC controller is tuned for a smaller desired inertia (for the target dynamics) $\mathbf{N} = \mathrm{diag}([0.008, \; 0.008, \; 0.0274]) \in \mathbb{R}^{3 \times 3}$, and then it is tuned for a bigger desired inertia $\mathbf{N} = \mathrm{diag}([0.03, \; 0.03, \; 0.0274]) \in \mathbb{R}^{3 \times 3}$, only around the $\mathbf{x}_B$ and $\mathbf{y}_B$ axes. Remember from Fig. 4 that the mass of the real system is $m = 1.49$ [kg], and its rotational inertia is $\mathbf{M}_{qr} = \mathrm{diag}([0.01708, \; 0.0172, \; 0.0274]) \in \mathbb{R}^{3 \times 3}$.

The results are given on the bottom of Fig. 7. For brevity, we only show the response of the second order rotational dynamics to the external torque around the $\mathbf{y}_B$ axis. In the figure, superscript $*^s$ stands for the measurements of

the *smaller desired inertia* case, while $*^b$ for the *bigger desired inertia* one. Notice that the external torques for both cases (i.e., $\tau_{e_y}^s, \tau_{e_y}^b$, depicted with black solid and dashed magenta lines, respectively) are the same. However the pitch orientations (i.e. θ^s, θ^b, depicted with gold and purple solid lines, respectively) are different from each other. Due to the position tracker implemented together with IDA-PBC (see Fig. 6), in both cases quadrotor comes back to its equilibrium after the disturbances. This creates a virtual rotational spring effect, making the system oscillate around its equilibrium until it reaches to a region of attraction. Notice the difference between the settling times of the two different cases; when the desired inertia is bigger, it takes longer for the system to reach its steady state than when the desired inertia is smaller. This is in line with the fact that for a rotational mass-spring-damper system with constant spring[18], coming back to its equilibrium would take longer when the rotational mass is greater.

This experiment and its results can be imagined for a human-robot physical interaction scenario, where we wish the flying robot to be able to physically interact with a human, and return to its equilibrium position as swift as possible. In such case one should aim at a flying robot with a smaller inertia than the original system has. Our controller provides here a controlled system with a desired physical interactive behavior.

4.5   *Sliding on an Uneven Ceiling Surface*

Here we present some experimental results of the quadrotor+rigid tool setup, sliding on an uneven ceiling surface. The purpose of the experiments is to show that by reshaping the inertia of the system using our proposed method, we can change the performance of the aerial physical interaction task, e.g., letting the quadrotor slide on the ceiling surface with a better contact profile.

The quadrotor+rigid tool setup is controlled using the method depicted in Fig. 6, where the system is steered via joystick commands, which are provided by a human observer. Although the physical interaction is controlled autonomously, by bringing the human in to the loop we aim at bringing some level of security to the system for avoiding an unexpected crash, and also pave the way for future human-in-the-loop experiments for APhI. The latter one is especially in the scope of our future research, by considering the utilization of a haptic device, which allows bilateral control of the robot (see Franchi et al. (2012)).

The results of the experiments are given in Fig. 8. There, we compare two cases: quadrotor controlled with a small desired inertia, i.e., $\mathbf{N} = \mathrm{diag}([0.004, \ 0.004, \ 0.0274]) \in \mathbb{R}^{3\times3}$, and with a big desired inertia, i.e., $\mathbf{N} = \mathrm{diag}([0.014, \ 0.014, \ 0.0274]) \in \mathbb{R}^{3\times3}$. Notice that the desired inertias are assigned only around $\mathbf{x}_B$ and $\mathbf{y}_B$ axes, while for the rotations around $\mathbf{z}_B$ it is same as the original system. On the top of Fig. 8 several snapshots from the experiments are given, where; (a) the quadrotor+rigid tool is first time in contact with the ceiling surface, (b) it is sliding on the even part of the ceiling, (c) just before the dent, (d) right after the dent, (e) just before a bulge which is built smoothly, (f) right after the bulge[19].

On the bottom of the figure the results are given, where gold solid curves stand for the response of the system with

smaller desired inertia, and the purple solid curves for the one with bigger desired inertia. The contact forces acquired from the F/T sensor along the **z**-axis are given as the first plot, and below it the z_q position of the quadrotor. Two plots in the second column show the roll (ϕ) and pitch (θ) values. Notice that the system with a bigger desired inertia (purple) preserves its contact with the ceiling much better than the one with a smaller desired inertia (gold), despite the uneven profile of the surface. A smaller desired inertia, in this case $\mathbf{N} = \mathrm{diag}([0.004, \ 0.004, \ 0.0274]) \in \mathbb{R}^{3\times3}$, causes more oscillations for the system along the $\mathbf{z}_W$ axis (z_q, up and down) and also around its rotational axes (see ϕ, θ). When we implement the controller to obtain a bigger desired inertia, i.e., $\mathbf{N} = \mathrm{diag}([0.014, \ 0.014, \ 0.0274]) \in \mathbb{R}^{3\times3}$, these oscillations are reduced and the contact with the surface during sliding became much better (notice especially the plot of the contact forces in Fig. 8). This result is in line with the numerical simulations of both Yüksel et al. (2014b) and Yüksel et al. (2014a).

This experiment and its results can be interpreted as a robot-environment physical interaction scenario, where we wish the flying robot to slide on a ceiling surface, e.g., for cleaning or painting task. In such case we might wish for a flying robot with a greater inertia than the original system has, and our proposed method can provide this while ensuring the passivity (with strong implication of stability) of the controlled system.

We note that in Fig. 8, even when the system is controlled for a bigger desired inertia, some small oscillations appear during the contact. This can be further improved by shaping the dissipation of the system, changing e.g., k_T, given in (26).

We refer the reader to the video attachment of this paper for a better visualization of the experimental results.

5   Conclusions

In this paper we presented an IDA-PBC method for reshaping the physical properties of a quadrotor, its robustness analysis and its first experimental results for different APhI tasks. For performing APhI the controller requires the knowledge of the external forces and torques, and in this paper we implemented and discussed two methods; (indirect) estimation and (direct) measurement of the external wrenches. Although each method overcomes another for different reasons, we chose to use a light-weight low cost 6D F/T sensor on board of a quadrotor for APhI, because of the results presented in Fig. 5, and considering future outdoor APhI applications. To our best knowledge, this is the first time in the literature that a quadrotor is flying freely and performing APhI task, with a 6D F/T sensor and its complete electronics on board of this flying platform. Moreover, first time in the literature we present the experimental results of controlling a quadrotor with IDA-PBC for APhI, in which the system is sliding on an uneven ceiling surface. This task can be interpreted in a later stage as surface inspection, painting or cleaning.

There are several possible future extensions of this work. First of all, so far we did not really take advantage of the high-level control input $\mathbf{u}_o$, except the way shown in Section 4.3. The employment of this control input,
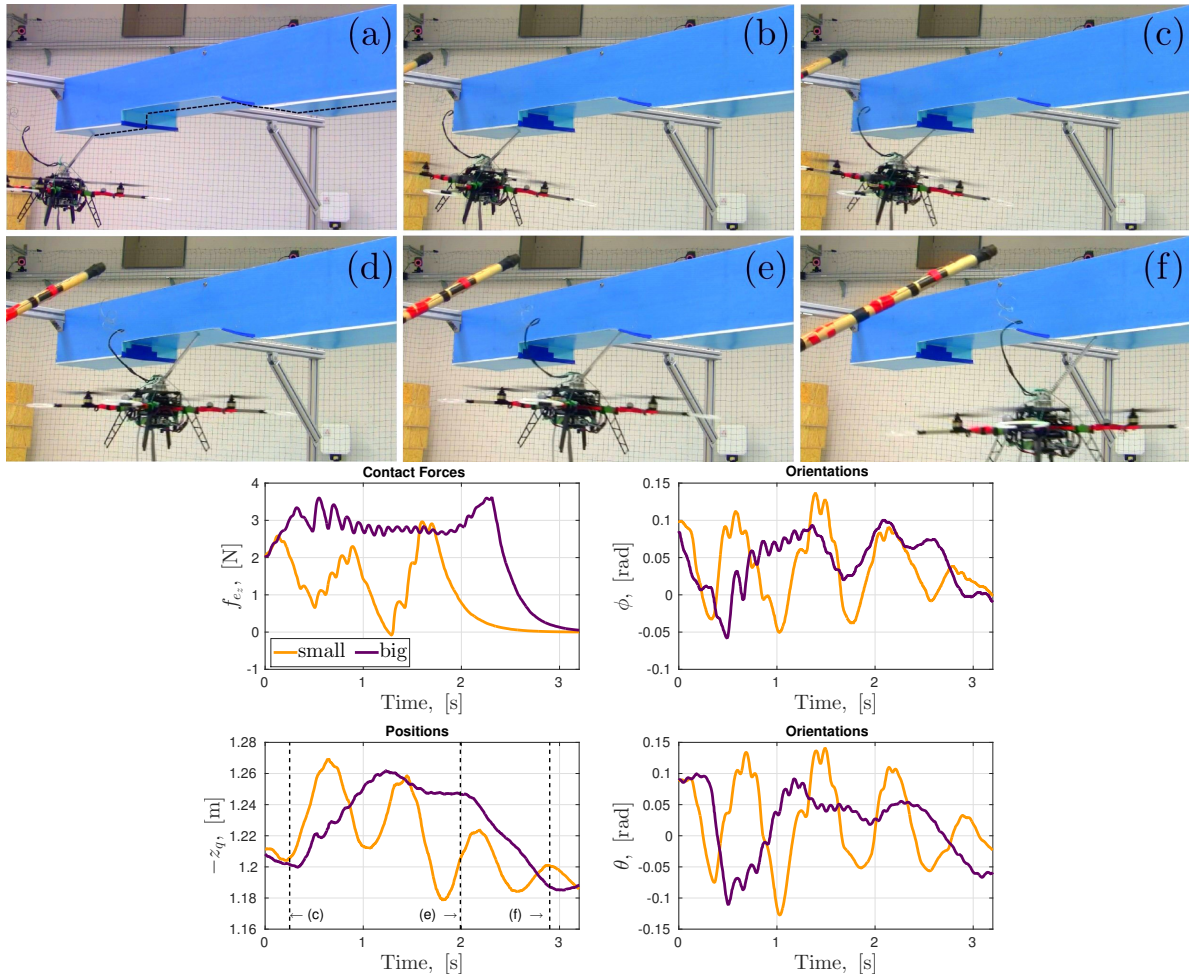
Figure 8. – *Top:* A series of snapshots (from (a) to (f)) from the experiments. The quadrotor setup as shown in Fig. 4 is sliding on a blue-colored uneven ceiling surface. The tip of the rigid tool is in contact with the ceiling, and its bottom is rigidly attached to the F/T sensor and the quadrotor body frame. The overall system is secured with a *slack* cable connected to a stick, for avoiding any dangerous crashes.
– *Bottom:* Experimental results for a quadrotor+rigid tool sliding on an uneven surface. Results for the system with the smaller desired inertia are depicted with gold curves, and the one with bigger desired inertia with purple curves. Three important time instants for z_q are highlighted with black dashed vertical lines; the moment before the dent (c), at the end of the dent and before the bulge (e), and the moment at the end of the bulge (f). Clearly, the system with bigger desired inertia follows the profile of the ceiling better than the one with the smaller desired inertia.

for e.g., force/torque tracking, or accounting noise effects mentioned in Section 2.4, is in the scope of our future works. Furthermore, looking at the results in Fig. 8, the contact profile with an uneven surface during sliding can be further improved, by changing the dissipative parameters, e.g., k_T, and also the desired mass m_d, but considering the limitations imposed by the robustness analysis from Section 2.4.

Acknowledgements

Notes

1. Potential energy is only one of the factors affecting the way a mechanical system interacts with the environment. Inertial properties and damping also play a major role for determining the interactive behavior. Furthermore, since the direction of the thrust of a quadrotor depends on the orientation of the system, it is not sufficient to shape the Cartesian impedance for achieving

an effective control of interaction. In light of this, we improved this controller in Yüksel et al. (2014b), which is recalled and reformulated in Section 2.

2. Even though IDA-PBC has been extended to generic affine systems in Astolfi and Ortega (2009), starting from a port-Hamiltonian dynamics is helpful for achieving simpler matching equations.

3. i.e. it is a positive definite differentiable energy function with a minimum at the desired equilibrium.

4. Notice that the robustness of the pre-compensating control input in (8) was evidenced in Section III of Lee et al. (2013)

5. Clearly from (49), the noises on the other states do not affect the wrench compensating control input.

6. Notice that the external wrench information acquired from different parts of the robot except its CoM can still be used for the IDA-PBC framework presented in Section 2 by applying rigid transformations. Also notice that the control as well can be reformulated for points of interest different than the CoM.

7. This implies the following: from the force/torque sensor we get $\tilde{\mathbf{w}}_s \in \mathbb{R}^6$ which is naturally given in the sensors body frame,

$\mathcal{F}_S$. However for our convenience we want to transform it to $\mathbf{w}_s$ defined in $\mathcal{F}_{Sb}$, because it has the same orientation as the body frame of the quadrotor. To do so, we apply (70).

8. Notice that if $\bar{\mathbf{d}}_l$ is the distance between P_T and P_S in $\mathcal{F}_S$, then according to Fig. 3 it is true that $\mathbf{d}_l = \mathbf{R}_S^B \bar{\mathbf{d}}_l$, where $\bar{\mathbf{d}}_l = [0.2\ 0\ 0.15]^T$ [m].

9. Notice the zoomed grayed-out parts of the figure, which are clearly showing the superior performance of the F/T sensor measurements over the estimations. Although the estimation performance can be improved by better tuning, this would be a model dependent approach, which might be a challenging task if the system is hard to model.

10. http://www.mikrokopter.de/en/home

11. http://wiki.mikrokopter.de/en/BL-Ctrl_2.0

12. https://git.openrobots.org/projects/tk3-mikrokopter

13. http://robotpkg.openrobots.org/robotpkg/localization/pom-genom3/index.html

14. https://redmine.laas.fr/projects/byueksel/repository/ftsens_iit

15. http://wiki.icub.org/wiki/FT_sensor

16. https://svn.tuebingen.mpg.de/humus-telekyb/hydro/trunk/packages/telekyb_users/tk_byueksel/src/ftsens_subpub.cpp

17. https://svn.tuebingen.mpg.de/humus-telekyb/hydro/trunk/packages/telekyb_users/tk_byueksel/

18. Note that the spring effect is due to the choice of the rotational desired inertia $\bar{V}_d$, damping is due to the damping injection implemented inside of the IDA-PBC, and the angular mass is the desired inertia $\mathbf{N}$.

19. Notice that the experiments are performed in a limited environment, since the artificial ceiling we have built in-home has a limited size (1.73 [m] in longitudinal). On the other hand, this was not the case for the simulations of Yüksel et al. (2014b), where the quadrotor was able to slide on a surface for couple hundreds of meters.

References

Acosta JA, Sanchez MI and Ollero A (2014) Robust control of underactuated aerial manipulators via ida-pbc. In: *2014 IEEE Conf. on Decision and Control*. Los Angeles, California, pp. 673–678.

Astolfi A and Ortega R (2009) Dynamic extension is unnecessary for stabilization via interconnection and damping assignment passivity-based control. *Systems & Control Letters* 58(2): 133 − 135.

Augugliaro F and DAndrea R (2013) Admittance control for physical human-quadrocopter interaction. In: *12th European Control Conference*. Zurich, Switzerland, pp. 1805–1810.

Bellens S, De Schutter J and Bruyninckx H (2012) A hybrid pose/wrench control framework for quadrotor helicopters. In: *2012 IEEE Int. Conf. on Robotics and Automation*. St.Paul, MN, pp. 2269–2274.

Cai G, Dias J and Seneviratne L (2014) A survey of small-scale unmanned aerial vehicles: Recent advances nd future development trends. *Unmanned Systems* 2(2): 1–25.

Chen W, Ballance DJ, Gawthrop PJ and O'Reilly J (2000) A nonlinear disturbance observer for robotic manipulators. *IEEE Trans. on Industrial Electronics* 47(4): 932–938.

Fantoni I and Lozano R (2002) *Non-linear Control for Underactuated Mechanical Systems*. Springer. ISBN 978-1447101772.

Franchi A and Mallet A (2017) Adaptive closed-loop speed control of BLDC motors with applications to multi-rotor aerial vehicles. In: *2017 IEEE Int. Conf. on Robotics and Automation*. Singapore, pp. 5203–5208.

Franchi A, Secchi C, Ryll M, Bülthoff HH and Robuffo Giordano P (2012) Shared control: Balancing autonomy and human assistance with a group of quadrotor UAVs. *IEEE Robotics & Automation Magazine, Special Issue on Aerial Robotics and the Quadrotor Platform* 19(3): 57–68.

Fumagalli M, Ivaldi S, Randazzo M, Natale L, Metta G, Sandini G and Nori F (2012a) Force feedback exploiting tactile and proximal force/torque sensing. *Autonomous Robots* 33: 381398.

Fumagalli M, Naldi R, Macchelli A, Carloni R, Stramigioli S and Marconi L (2012b) Modeling and control of a flying robot for contact inspection. In: *2012 IEEE/RSJ Int. Conf. on Intelligent Robots and Systems*. Vilamoura, Portugal, pp. 3532–3537.

Gioioso G, Ryll M, Prattichizzo D, Bülthoff HH and Franchi A (2014) Turning a near-hovering controlled quadrotor into a 3D force effector. In: *2014 IEEE Int. Conf. on Robotics and Automation*. Hong Kong, China, pp. 6278–6284.

Grabe V, Riedel M, Bülthoff HH, Robuffo Giordano P and Franchi A (2013) The TeleKyb framework for a modular and extendible ROS-based quadrotor control. In: *6th European Conference on Mobile Robots*. Barcelona, Spain, pp. 19–25.

Guerrero ME, Mercado DA, Lozano R and Garcia CD (2015) Passivity based control for a quadrotor uav transporting a cable-suspended payload with minimum swing. In: *2015 IEEE Conf. on Decision and Control*. Osaka, Japan, pp. 6718–6723.

Ha C, Lee DJ and Nguyen HN (2015) Mechanics and control of quadrotors for tool operation. *Automatica* 61: 289301.

Khalil HK (2001) *Nonlinear Systems*. 3rd edition. Prentice Hall. ISBN 978-0130673893.

Lee DJ, Franchi A, Son HI, Bülthoff HH and Robuffo Giordano P (2013) Semi-autonomous haptic teleoperation control architecture of multiple unmanned aerial vehicles. *IEEE/ASME Trans. on Mechatronics, Focused Section on Aerospace Mechatronics* 18(4): 1334–1345.

Mahony R, Beard RW and Kumar V (2016) *Modeling and Control of Aerial Robots*. Springer. ISBN 978-3-319-32552-1, pp. 1307–1334. DOI:10.1007/978-3-319-32552-1_52. URL http://dx.doi.org/10.1007/978-3-319-32552-1_52.

McKinnon CD and Schoellig AP (2016) Unscented external force and torque estimation for quadrotors. In: *arXiv*. URL https://arxiv.org/abs/1603.02772.

Mersha AY, Carloni R and Stramigioli S (2011) Port-based modeling and control of underactuated aerial vehicles. In: *2011 IEEE Int. Conf. on Robotics and Automation*. Shanghai, China, pp. 14–19.

Naldi R (2008) Prototyping, modeling and control of a class of vtol aerial robots. Doctorate Thesis, University of Bologna.

Naldi R, Gentili L, Marconi L and Sala A (2010) Design and experimental validation of a nonlinear control law for a ducted-fan miniature aerial vehicle. *Control Engineering Practice* 18(7): 747–760.

Nguyen H and Lee D (2013) Hybrid force/motion control and internal dynamics of quadrotors for tool operation. In: *2013 IEEE/RSJ Int. Conf. on Intelligent Robots and Systems*. Tokyo, Japan, pp. 3458–3464.

Nikoobin A and Haghighi R (2009) Lyapunov-based nonlinear disturbance observer for serial n-link robot manipulators. *Journal of Intelligent & Robotics Systems* 55(2-3): 135–153.

Ortega R, van der Schaft A, Maschke B and Escobar G (2002) Interconnection and damping assignment passivity-based control of port-controlled Hamiltonian systems. *Automatica* 38(4): 585–596.

Ruggiero F, Cacace J, Sadeghian H and Lippiello V (2014) Impedance control of VToL UAVs with a momentum-based external generalized forces estimator. In: *2014 IEEE Int. Conf. on Robotics and Automation*. Hong Kong, China, pp. 2093–2099.

Schiano F, Alonso-Mora J, Rudin K, Beardsley P and Siciliano RB (2014) Towards estimation and correction of wind effects on a quadrotor uav. In: *IMAV 2014: International Micro Air Vehicle Conference and Competition*. Delft, Netherlands.

Secchi C, Stramigioli S and Fantuzzi C (2007) *Control of Interactive Robotic Interfaces: a port-Hamiltonian Approach*. Tracts in Advanced Robotics. Springer. ISBN 978-3540497127.

Sepulchre R, Jankovic M and Kokotovic P (1997) *Constructive Nonlinear Control*. Communications and Control Engineering Series. Springer. ISBN 3540761276.

Siciliano B and Khatib O (2008) *Handbook of Robotics*. Springer. ISBN 9783540382195.

Spong MW (1998) Underactuated mechanical systems. In: Siciliano B and Valavanis KP (eds.) *Control Problems in Robotics and Automation*. Springer, pp. 135–150.

Tomic T and Haddadin S (2014) A unified framework for external wrench estimation, interaction control and collision reflexes for flying robots. In: *2014 IEEE/RSJ Int. Conf. on Intelligent Robots and Systems*. pp. 4197–4204.

Wang Z, Goldsmith P and Gu J (2009) Regulation control of underactuated mechanical systems based on a new matching equation of port-controlled Hamiltonian systems. In: *2009 IEEE Int. Conf. on Robotics and Automation*. Kobe, Japan, pp. 992–997.

Willems JC (1972) Dissipative dynamical systems part I: General theory. *Archive for Rational Mechanics and Analysis* 45(5): 321–351.

Yu Y and Ding X (2012) A quadrotor test bench for six degree of freedom flight. *Journal of Intelligent & Robotics Systems* 68(3): 323338.

Yüksel B (2017) *Design, Modeling and Control of Aerial Robots for Physical Interaction and Manipulation*. Logos Verlag Berlin. ISBN 978-3-8325-4492-8.

Yüksel B, Secchi C, Bülthoff HH and Franchi A (2014a) A nonlinear force observer for quadrotors and application to physical interactive tasks. In: *2014 IEEE/ASME Int. Conf. on Advanced Intelligent Mechatronics*. Besançon, France, pp. 433–440.

Yüksel B, Secchi C, Bülthoff HH and Franchi A (2014b) Reshaping the physical properties of a quadrotor through IDA-PBC and its application to aerial physical interaction. In: *2014 IEEE Int. Conf. on Robotics and Automation*. Hong Kong, China, pp. 6258–6265.

Zhan X (2006) Extremal eigenvalues of real symmetric matrices with entries in an interval. *SIAM Journal on Matrix Analysis and Applications* 27(3): 851–860.